A BIOLOGICALLY INSPIRED METHODOLOGY FOR MULTI-DISCIPLINARY TOPOLOGY OPTIMIZATION

A THESIS SUBMITTED TO THE
GRADUATE DIVISION OF THE
UNIVERSITY OF HAWAI'I AT MĀNOA
IN PARTIAL FULFILLMENT OF THE
REQUIREMENTS FOR THE DEGREE OF

MASTER OF SCIENCE

IN

MECHANICAL ENGINEERING

MAY 2012

By

NADINE YUMI KAWABATA

Thesis Committee:

Marcelo H. Kobayashi, Chairperson
Monique Chyba
Weilin Qu

We certify that we have read this thesis and that, in our opinion, it is satisfactory in scope and quality as a thesis for the degree of Master of Science in MECHANICAL ENGINEERING .

THESIS COMMITTEE

_____

Chairperson

_____

_____

ACKNOWLEDGMENTS

First and foremost I would like to express my gratitude to my advisor Dr.Marcelo Kobayashi for his guidance and support throughout my experience in the mechanical engineering program. He has not only given me the great opportunity to pursue this research, but has inspired me with his great passion for lifelong learning.

I would also like to thank a number of other individuals who have provided me with enormous help along the way. I would like to acknowledge my committee members Dr.Monique Chyba and Dr.Weilin Qu for their time and mentoring in the completion of my thesis. Thank you to Adam Kearney, Nathan Shimabuku, and all my colleagues for their endless friendship, advice, and assistance. Lastly, nothing would be possible without the love and support of my family which I am forever grateful for.

The research work in this thesis was funded in part by the Air Force Office of Scientific Research through Grant No. FA9550- 10-1-0036.

ABSTRACT

This thesis introduces a biologically inspired topology optimization method with the incorporation of fractones. The proposed method was adapted from a current optimization method which employs a cellular division model for the generation of topological maps. Once topologies are generated, they are evaluated for a set of performance functions and optimized through a genetic algorithm. The proposition of this thesis was that the incorporation of fractones into the existing mapping system may improve the overall efficiency and performance of the optimization algorithm. Fractones are small extracellular structures believed to regulate the cellular division process through the capture and transport of growth factors. In this model the distribution and diffusion of growth factors served as additional control parameters in the creation and optimization of topologies. Both the fractone modified and original methods of the mapping system were applied to an aeroelastic flapping membrane wing optimization problem in which the supporting lattice structures of the wings were optimized for power requirement, lift, and thrust performances. The performances of the original and fractone models were compared and analyses of the generated venation patters were made.

Keywords: Multidisciplinary Design Optimization, Map *L*-system, Biologically Inspired Structures, Fractones.

TABLE OF CONTENTS

LIST OF TABLES

LIST OF FIGURES

CHAPTER 1
INTRODUCTION

Topology optimization is the critical field of engineering which aims at optimizing the material distribution in a given domain such that a set of boundary conditions are satisfied and a set of performance targets are approached. These techniques are often useful in industries for reducing the costs of design and preliminary modeling. There are a number of purposed methods for topology optimization and many of the common methods include a genetic algorithm for optimization and finite element schemes for evaluation of the design candidates.

Solid isotopic material with penalization for intermediate densities (SIMP) [1] [2] is one popular method for topology optimization. This approach uses a discretized domain with grey scale elements. Rather than strictly solid material and void elements in the design domain, the elements are allowed to range on a 0 to 1 scale. The resulting structures however, are difficult to manufacture or not feasible in many cases. To remedy this problem, a penalization value is assigned and this penalization serves to bias the structure toward purely solid and void elements. Appropriate selection of the penalization value is crucial to the performance of this method and is often considered the short fall of this algorithm. Substantial penalization is needed to avoid large areas of grey, but too large of a penalization may produce local optima. The quality of the optimized design obtained with the SIMP method is also strongly dependent on the smoothness of the objective function and the constraints. In addition, the numerical method for obtaining a solution for the SIMP method becomes increasingly unstable for highly non-linear problems.

Genetic algorithms are preferred to the previous method for its versatility, ability to handle complex problems, and gradient free nature. Simple examples of genetic algorithms directly correlate the genome of a design to the structure. Here each gene is a binary unit that corresponds to a solid or void element in the discretized domain [3]. The difficulty of this approach is that refined grids are often required for meaningful results; however this

increases the computational demands and slows convergence. Many of the designs generated in this manner are also unfeasible due to occurrences such as checker boarding and island formations [4]. To avoid these problems, this work uses a genetic algorithm that encodes a cellular division mapping model [5] [6]. This model generates simple connected structures so that resolution and connectivity obstacles are removed. The nature of the mapping system also requires a relatively small set of genes, yet presents a vast pool of potential designs.

1.1 Research Objectives

This thesis is aimed at the development of a new methodology for topology optimization. This work adapts the existing biologically inspired algorithm which models the cellular division process to generate topological maps. Previous work has been done to incorporate this cellular division model to create topologies for a given design problem and optimize the resulting designs in a genetic algorithm. This process so far has proven successful results.

The proposal here is to improve the existing system through modifications of the biological model that is the basis of forming the topologies. More specifically, the goal is to improve the results of the topology generation algorithm by adding additional control parameters to bias the generated designs to better suit the demands of the design problem. This is accomplished by implementing another biological phenomenon known as fractones[7] [8] [9].

Fractones, a fairly recent biological finding, are an extracellular structure believed to have the ability to govern the location and occurrence of cellular divisions. While fractones govern where and when the cell divides, the fractones themselves are regulated by a number of chemicals called growth factors. As these chemicals diffuse, they are captured by the fractones and when the fractones reach a threshold value of the growth factors, they initiate a cellular division.

To incorporate the idea of fractones, the topologies here evolve by simulating the diffusion of growth factors along the members of the initial map. A number of fractones are fixed along the members and once they reach a predefined value of diffusing growth factors,

they initiate a new division (creation of a new beam) in the design. The distribution of growth factors, the rate of diffusivity, and the threshold values in the scheme influence the final topology generated. These modifications may have a number of potential benefits, including an improved rate of convergence and more optimal designs. The methods are tested here on a flapping membrane wing optimization test problem.

CHAPTER 2
METHODS

This chapter will address a number of background areas including: the mapping model which simulates cellular divisions, the recent finding in the field of neurobiology, known as fractones, a novel topology optimization method, and an aeroelastic flapping wing optimization problem. The first two crucial elements, fractones and the mapping algorithm, will initially be discussed as distinct and independent topics, and later brought together to introduce a new model for topology optimization. The motivation and mechanisms of the proposed model will be described in detail and followed by the description of a specific engineering application which will be used for validation.

The organization of this chapter will begin with a definition of the map L-system which is used to generate the topological maps in section 2.1. This section will then be followed by a closer look into the biological field of cellular division and the inspiration for the methods developed here, called fractones, in section 2.2. The two preceding sections will then merge in section 2.3, where the fractone map L-system will be introduced. The manner in which the fractones are modeled along with the diffusion of their associated growth factors will be discussed, along with its implementation in the original map L-system. Finally, the novel method presented will be applied to a sample problem of a flapping membrane wing optimization which will be addressed in section 2.4.

2.1 Map *L*-system

Introduced in 1968 by biologist Aristid Lindenmayer, the Lindenmayer system (or L-system) is a method of rewriting a series of character/grammar strings in a parallel fashion. The versatility of the L-system to represent the parameters of any starting element with a character string and evolve the structure by implementation of the governing production rules has proven the system to be useful for a number of applications. Some applications include the ability to produce interesting fractal geometries, model the branching growth

of plant structures, and simulate cellular divisions (some examples may be seen in figure 2.1). The map L-system [10] [11], proposed by Nakamura, Lindenmayer, and Aizawa, is the extension of the algorithm which models single layer cellular divisions and is the basis for the topologies generated in this work.

Maps are planar graphs defined by a finite set of regions in which each region is enclosed by a string of edges which meet at vertices. Every edge has one or two associated vertices, all edges are a part of a region's boundary, and all edges are connected (such that there are no island formations). A map may be representative of a single cellular layer where the edges are the cell wall, the enclosed regions are the intracellular space within the cells and the extracellular spaces are omitted. Simultaneous cell divisions are modeled with a binary propagating map 0L system with markers (or mBPM0L-system). The 0L system is the context-free Lindenmayer parallel rewriting system in which there are no interactions between cells. The map L-system is binary and propagating because cells are always divided into two daughter cells and in this model cells are never destroyed or joined. The markers play the functional role of flagging the boundary edges at potential vertices where the cell may divide and new edges may form [10].

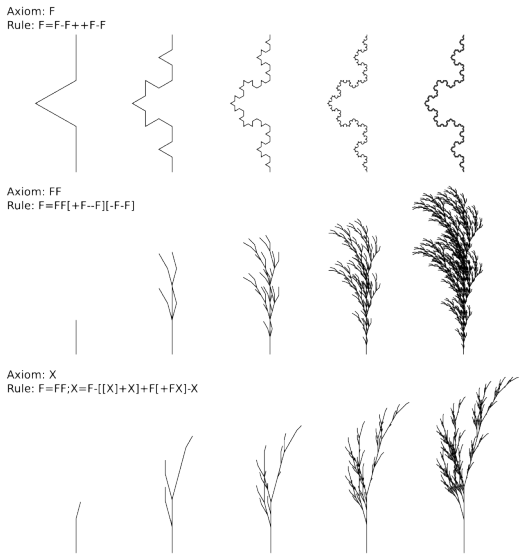

Figure 2.1: Sample images generated by L-systems: fractal pattern (top), development of plant structures (mid and bottom)

In overview, a two dimensional map L-system is first initiated with an axiom that defines the edges of the domain. Once initiated, the closed map undergoes a series of subdivisions by the addition of straight internal edges. The creation and location of these edges are governed by a predefined set of production rules. The algorithm begins each iteration with a discretization of the existing edges of the map and a placement of markers at selected nodes. The discretization patterns of the edges and the location and orientation of markers

are based on the production rules. Once all edges have been divided and markers placed, the new edges are created by matching the markers. When two markers are present along the boundary of a common region, have the same label, and appropriate orientations, they will form a new wall between the two markers.

A simple example of a map L-system may perhaps be best expressed in its mathematical form. The system is first defined an alphabet, Σ, which is a finite set of characters (letters and symbols) and may be represented as $\Sigma = \{A, B, C, ..., [,], +, -\}$. From this alphabet, characters are selected to create an axiom, Ω, which is the string that initiates the rewriting process. Here the axiom will be selected as $\Omega = ABAB$. The third and final item required is the finite set of production rules or rewriting rules, P. The production rules are also limited to the characters of the alphabet, Σ, and must take the form $\alpha \rightarrow \chi$. α is a single character of the alphabet which serves as the predecessor and χ is the word (or string) called the successor. Note that if there are multiple rules with identical predecessors and differing successors, a probability may be assigned to each rule to determine the frequency at which each are utilized. For this example the set will consist of two production rules:

$$\begin{aligned} A &\rightarrow B[-A]x[+A]B \\ B &\rightarrow A \end{aligned}$$

To this point, the example is nearly a simple D0L-system (deterministic because the predecessors are non-repeating and context free) which is not specific to a map generation. The example put forth however, may be applied to a mapping problem with the addition of a few rules.

In a mapping scenario, each letter of the axiom represents an edge of the initial map. Therefore the length of the axiom must be equal to the number of edges in the initial structure. It is also customary to include the special characters [,], +, and - when using a map L-system. When included in the production rules, the matching brackets, [and], indicate the inclusion of a marker which is labeled by the enclosed character. The orientation

(+ or -) preceding the label in the closed brackets indicates the directionality of the marker, in this case the + symbol correlates to a counterclockwise placement of the edge. The remaining characters of the successor, which are not enclosed by brackets, indicate the number of segments the preceding edge is divided into. The new edges will be labeled as prescribed by the rules and nodes are placed between the edges. For example the first edge, A, which is the lower boundary of the map in figure 2.2, is discretized into three equal segments. The new edge segments are labeled, B, x, and B respectively. Between the first and second segments a marker oriented downward is placed and an upward oriented marker is placed between the second and third segments. Since the first marker is oriented outward from the map it is discarded while the second marker is eventually paired with the other inward facing marker on the upper boundary.

After all the pertaining edges are subdivided and markers are placed, the markers are checked for any possible pairings. As mentioned earlier, a pair of markers are matched if they belong to the same cell (are on the boundary of the same region), are not located on the same edge, if their labels are the same, and if they are oriented toward each other. There may be more than one potential set of marker pairs in a given cell, but the first pair to be found determines the location of the cell division. After cells are scanned for matching markers and the locations of the cellular divisions are determined, the remaining markers are discarded. The resulting maps generated in this example, for an initial square map with equal subdivisions of the edges, are shown in figure 2.2.

For the purpose of generating and optimizing topological maps in engineering applications it is practical to enforce a few additional constraints. After satisfying the previous conditions to create a cell wall, an eligible marker pair and its respective new edge must also meet certain limits prescribed by the user:

1. Prevention of small angles: the angles between the adjacent edges in the divided cells must be larger than a prescribed lower limit; this prevents the creation of cells with narrow angles.

2. Prevention of small areas: each newly formed cell must have a regional area which

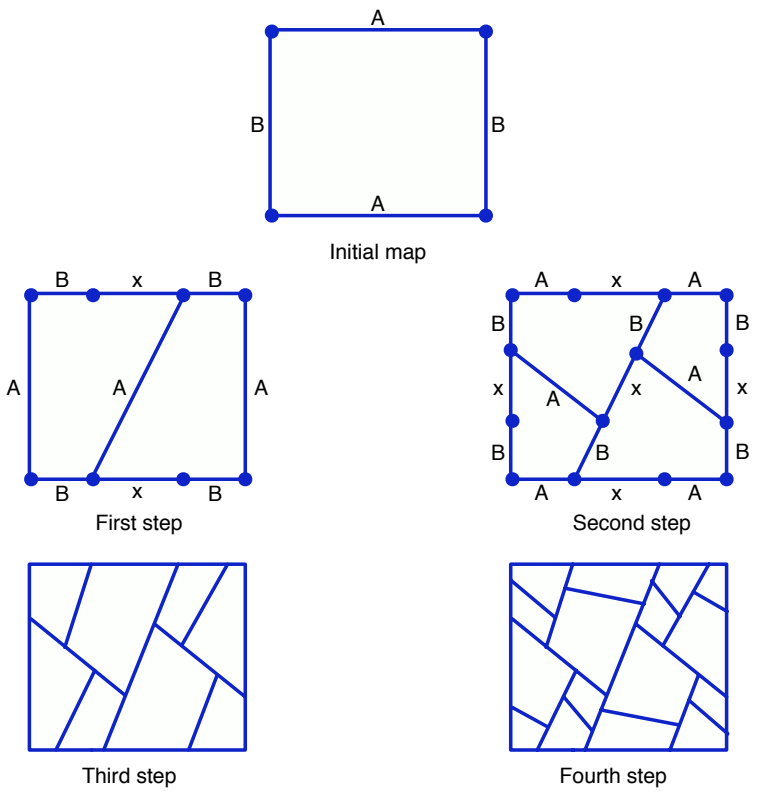

Figure 2.2: Example of the mBPMOL-systems process for the first four iterations where $\Omega = ABABand$ P: $A \rightarrow B[-A]x[+A]B$ and $B \rightarrow A$.

is greater than a prescribed percentage of the original map to avoid the formation of excessively small regions.

For practical problems, the structure must also have a finite number of edges. In some cases the cell divisions will cease when all edges of the map are labeled with a terminal token such (such as x in the previous example). Otherwise there exists a maximum number of iterations to be completed. Since this value is highly variable and dependent on the problem at hand, a number of iterations may be prescribed at the start of the map generation program or optimized in the genetic algorithm.

This section has provided a brief introduction to L-systems and an overview of the map L-system as is pertinent to topological map generations. For more details and information on Lindenmayer systems, the reader is referred to [10] and the references there in. The next

section will further investigate the biological aspects of cellular division and their associated regulation mechanisms.

2.2 Fractones

In cellular biology the mitotic phase, or period of active cellular division, is generally a minor component of the overall cell cycle. A majority of the cell's time is rather spent in preparation for a cellular division, where accumulation of mass and nutrients and synthesis of DNA occurs. Cell cycles may also be dormant at times when inactive time gaps are included [12]. While rapid cellular division may take place in the early stages of life to promote growth of the individual, the main purpose of cellular divisions in adult organisms is for the maintenance of the body. Adult cellular divisions are reduced to the replacement of damaged and aged cells and to meet the overall functional needs of the individual. As a result, the frequency of cellular divisions is highly variable and dependent on the type of cell and the physical state of the body. To accommodate for these variable rates of demand, the cells will typically enter periods of arrest or dormancy until an external indicator is presented and initiates the division process.

For this engineering application, our interest lies in the regulation of the cell cycle. Many cells do not replicate very frequently and often branch from the cell cycle into a dormant phase until signaled to resume active division. In these cases the cell only begins to actively divide when initiated by an external source, most often by cell-type specific molecules known as growth factors. Our focus is in better understanding these control and regulation processes which govern the cell cycle and initiate cellular divisions. Recent findings in the area of neurosciences have introduced new concepts for better understanding such regulatory processes. The results of these studies, which will be reviewed in this section, are the inspiration for the model presented in this work.

In adult neurogenesis, neurons are generated from neural stem and progenitor cells (NSPC) . NSPC are localized in specific area of the brain, most notably the subependymal layer of the left ventricle [7] [8]. Neural stem cell differentiation and proliferation in these

areas are also known to be governed by the presence of growth factors, but the details of this regulatory process have remained unknown.

It has been hypothesized that the extracellular matrix in the adjacent regions of the left ventricle wall also plays a contributing role in the initiation of cellular divisions. Close examination of these regions have brought attention to branched structures in the extracellular matrix which come in direct contact with the NSPC. This branched (stem and bulb) structure which binds to the NSPC has assumed the term, fractones[7] [8]. Fractones are believed to be associated with the material of basement membranes which is the surface tissue containing high concentrations of extracellular molecules (ECM). These extracellular molecules include heparan sulfate proteoglycans (HSPG) which is a known binding cofactor of growth factors[7].

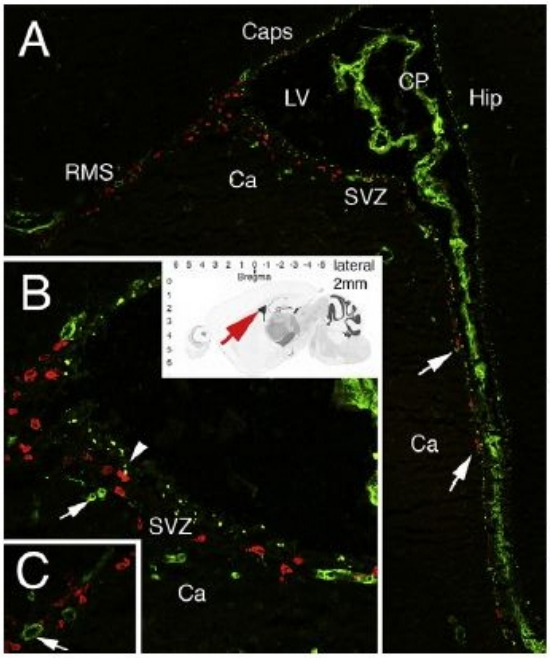

Figure 2.3: Cell proliferation and Fractones in the lateral ventricle: Fractones (arrows, green labeled N-sulfated HS) and proliferating cells (red labeled BrdU+) near the N-sulfated heparan sulfate fractone structures.

Imaging and statistical analysis methods have produced many new findings and evidence supporting the relationships theorized above. Molecules comprising the basement membranes have been identified in fractones structures, confirming that the two materials are indeed affiliated. A high density of cell proliferation was also observed near fractones, especially those containing N-sulfate HSPG[7]. Immunolabeling techniques were performed to identify cells recently entering mitosis in several dissection samples. It was found that the majority of cells initiating cellular division were in the areas adjacent to fractones and capillaries, however statistical analysis revealed that cells initiating mitosis were generally in closer proximity to fractones[7]. These results indicate that fractones store the fibrob-

last growth factor 2 (FGF-2) via binding with HSPG and they are the main structures in relaying FGF-2 (growth factors) to the neural stem cells which then undergo mitosis.

The introduction to fractones presented here express the basic concepts that are of interest in this work. For further details on the analysis of fractones refer to [7] and [8].

2.3 The Fractone Map L-system

Thus far the map L-system and fractones have been introduced individually. In this next segment, the map L-system will undergo modifications to incorporate the idea of fractones and generate the resulting fractone map L-system.

It was previously demonstrated that fractones play a vital role in initiating division of their associated cells through the capture and delivery of growth factors from the extracellular space to the eligible cell. The model proposed here utilizes a similar and slightly simplified concept. For the purposes of this study, fractones are modeled as small and stationary structures which passively capture and consume simply diffusing growth factors. The fractones initiate mitosis in its neighboring cell once a threshold quantity of the growth factors is accumulated. The rates of growth factor accumulation in these structures are governed by a constant diffusion coefficient and the initial distribution of the growth factor molecules.

Integration of the fractones into the map L-system is accomplished by the assumption that all of the previously introduced markers in the map L-system represent fractones. All boundary and internal nodes also indicate active fractones (corner nodes are neglected). For simplification it is assumed that all markers (i.e. fractones) are actively consuming growth factors and remain active for the remaining iterations of the map generation. The fractones also have the same affinity for growth factors, and all fractones have the same threshold value. There is only one type of growth factor present in this model and the diffusivity of the molecule is constant throughout the system.

The diffusion of the growth factors along the edges is approximated with a one dimensional, piecewise linear finite element scheme. Diffusion is modeled along each line segment

between markers and each segment is discretized with a constant number of uniform nodes. The source term of the diffusion equation is set to zero and the initial distribution of the growth factor is prescribed. All segment ends (fractone locations) are prescribed Dirichlet boundary conditions with a fixed concentration of zero.

The diffusion model is also prescribed a finite number of uniform time steps and after each time step, the amount of growth factors consumed at each node is computed. All eligible markers must accumulate the threshold value of growth factors in addition to satisfying all other requirements to form a pair and initiate a new cell wall formation. One example for such a case where the fractones influence the topology can be seen in figure 2.4.

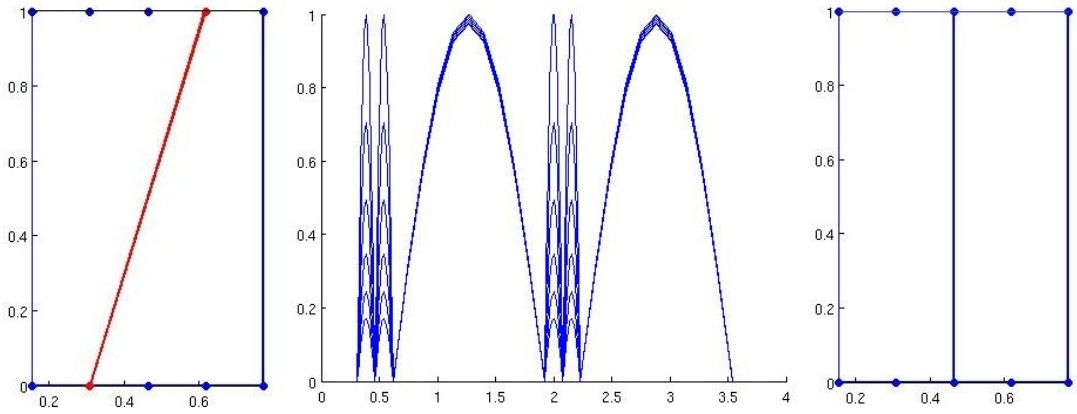

Figure 2.4: First iteration of a mapping with and without fractones with axiom: ABAB and production rules:A → B[+A]x[+A]x[+A]B and B→A: a) First subdivision using original mapping system b) Diffusion of growth factors along linearized edges of the map (starting at bottom edge): GF concentration vs. x c) First subdivision using fractone mapping system

After each iteration of the map generation when additional markers are placed and new walls may be formed, the growth factors are redistributed. For each existing segment that undergoes new subdivisions, the total quantity of growth factor is conserved and distributed among the new subsections. The existing growth factors of the edge are accumulated and dispersed with a weighted distribution governed by the length of each new segment. When a new wall is formed, an initial concentration of growth factors must also be assigned. In this case the average growth factor concentration of all existing segments is computed and

assigned to the newly formed wall segments. This averaging is performed to remove any bias of wall formations at this member due to extremely low or high concentrations of growth factors relative to the remaining edges.

The growth factor concentrations for these calculations are carried over from the previous iteration in the map generation. If a pair of markers were matched in the preceding iteration, the growth factor concentrations of all edges during the first time step in which both markers reached the threshold value, serve as the initial conditions for the next iteration of the map. If there were no matching pairs in the previous iteration, the growth factor concentrations along all the edges during the last time step are the values carried over to the next iteration of the map generation.

While this method is more complex and requires greater computational time to generate maps compared to the original map L-system, it has the potential to improve the overall performance of the optimization with the addition of the diffusion parameters in the genetic algorithm. This scheme may prove to be beneficial when applied to complex optimization problems such as the application presented in the next section.

2.4 Flapping Wing Optimization

An aeroelastic flapping membrane wing model [6] will serve as the test application of the above mentioned optimization methods. This problem analyzes the performance of a forward flight flapping membrane wing for a micro air vehicle. These bio-inspired wings are comprised of thin, flexible membranes reinforced with a rigid beam network, similar in form to the veined wings of insects. The performance of the wing structures are influenced by the venation patters of the supporting members and it is this topology which will undergo optimization. Both the original and fractone inspired map L-systems will be applied independently and the resulting maps will be used to generate the Pareto curves parameterized by the designs power requirement and thrust generation.

Evaluation of the wings under the given flight conditions are to be accomplished as follows. The structural modeling of the wing will be completed using a finite element

analysis of the membranes with a triangular mesh (figure 2.5). The respective governing equation is applied to each element of the membrane:

$$N_x \cdot w_{,xx} + 2N_xy \cdot w_{,xy} + N_y \cdot w_{,yy} + f_z(x, y, t) = \rho \cdot w_{,tt} \tag{2.1}$$

where N is the pre-stressed resultants, w and f are the out-of-plane displacement and applied force per area, and ρ is the membrane density per length. The Euler-Bernoulli equation is used to analyze the beam members (battens, leading edge, tip, and root) [6].

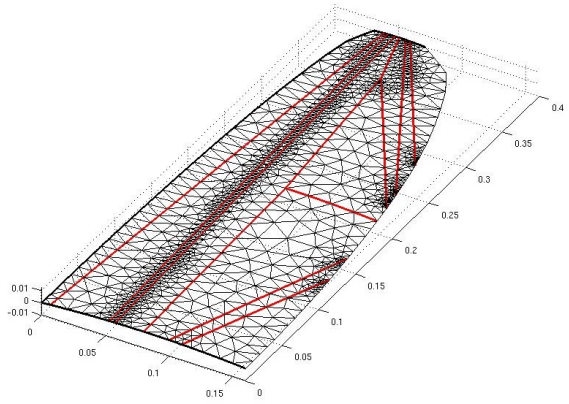

Figure 2.5: Finite element mesh of a sample wing design: triangular mesh of membrane, battens (red)

The governing equations are converted into the usual finite element matrix form:

$$M \cdot u'' + C \cdot u' + K \cdot u = F \tag{2.2}$$

where M is the mass matrix, C is the damping matrix, K is the stiffness matrix, F is the accumulated load vector, and u is the total deformation of the structure [6] [13]. Here the solution, u, is also approximated with a linear combination of modes:

$$u = \Phi \cdot \eta \tag{2.3}$$

where Φ is the modal matrix of natural vibrations and η is the modal amplitudes.

Prior to evaluating the performance of the wing designs, a few parameters must be defined. The flight kinematics are characterized by two angles of the wing, the first is the static angle of attack with respect to the external flow, α, and the second value, β, prescribes the range of the sinusoidal flapping. A constant velocity is also defined for the external air flow and a body attached coordinate system is utilized for the remaining computations.

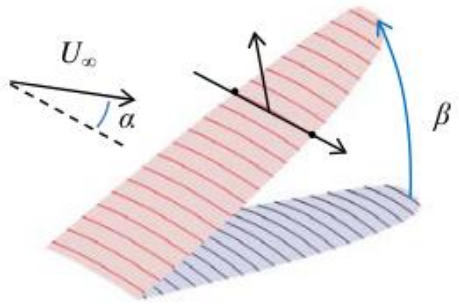

Figure 2.6: Characteristic angles and span-wise stations of the flapping wing with an attached coordinate system

The aerodynamic loads as opposed to the structural analysis are evaluated with a number of span-wise cross-sections of the wing. The pressure across the wing is determined by applying the no-penetration condition at each span-wise station:

$$\overline{\nu} + \lambda = u_o \cdot \frac{\partial h}{\partial x'} + \frac{\partial h}{\partial t} + \nu_o + \nu_1 \cdot x'/b \tag{2.4}$$

where h is the shape of the wing, u_o is the horizontal velocity, the last three terms are the vertical velocity (where b is the local semi-chord), and $\overline{\nu}$ and λ are the induced flow from the bound and trailing circulations [6]. The terms h, $\overline{\nu}$ and λ are transformed using the Glauert space $\varphi = acos(x'/b)$ for computations henceforth and the resulting integrations are computed using a defined set of Gaussian integration points.

The loads acting over each span section are computed using:

$$F_{y'} = \int_{-b}^{b} \Delta P \cdot dx' + F_{y'}^{\nu} \tag{2.5}$$

$$F_{x'} = \int_{-b}^{b} \Delta P \cdot \frac{\partial h}{\partial x'} \cdot dx' - 2\pi \cdot b \cdot \rho_\infty \cdot (nu_o + h_o - \lambda_o + u_o \cdot \Sigma n \cdot \frac{h_n}{b})^2 + F_{x'}^{\nu} \tag{2.6}$$

and the respective viscous terms are computed as follows ($F_{y'}^{v}$ is determined similarly):

$$F_{x'}^{v} = b \cdot \rho_i nfty \cdot U_\infty^2 \cdot (C_{D0} \cdot cos^2\alpha_s + C_{D\pi/2} \cdot sin^2\alpha_s) \cdot u_o / \sqrt{u_o^2 + v_o^2} \tag{2.7}$$

$$\alpha_s = atan(\frac{h(-b) - h(b)}{2b}) + atan(\frac{v_o}{u_o}) \tag{2.8}$$

where α_s is the local angle of attack, and C_{D0} and $C_D\pi/2$ are the drag coefficients at angles 0 and $\pi/2$ respectively.

A coupling of the two previous models (structural and airload) is employed to solve for the wing response at each temporal state. The loads are solved for at each cross-sectional segment and interpolated into the structural finite element mesh. The value of the pressure is evaluated at the center of each finite element and considered to be constant over the entire element. The deformation of the wing is determined and the wing shape is updated.

When the air vehicle is subjected to time-periodic flight conditions, the above solution may also be assumed to be time-periodic upon degradation of any transient terms. Each complete flapping cycle may therefore be discretized in time and the set of time-monolithic solutions are approximated using a finite element method.

Further details and information on evaluation of this model may be found in [6] and the references therein.

2.4.1 Genetic Algorithm

Once the topological maps have been generated by the previously discussed scheme, there is then the need for a system to evaluate, analyze and optimize the maps to produce useful results. Here the topologies are optimized using a genetic algorithm (GA). Just as biological evolution continues to progress by the process of natural selection, the nature of this method is to mimic the evolutionary process by preserving the most fit individuals. Genetic algorithms also allow for mutations and hybridization of individuals to produce

offspring, however the advantage here is that computational process is greatly accelerated compared to the conventional evolution process.

The genetic algorithm generally begins with strings of numbers (equal in length) which are analogous to genomes of a common species. Each numerical string represents one individual and the number of strings represents the population size, which is constant through each generation. The genomes are representative of the structures which are to be optimized; in this case each genome may be translated into a topological map by the (fractone) map L-system. The individual genes or elements of the string are used to generate the axiom and production rules associated with the map L-system. The first set of numbers in the genome is translated into the axiom, generating a character label and directionality for each initial edge of the map. The majority of the genes used occur in the second extraction from the genome. This set generates the production rules which again prescribe a number of character strings and associated orientations for the markers. In the case of the fractone map L-system, an additional three genes are placed at the tail of the genome. These last three genes contain the values for the threshold, diffusivity, and initial concentration of the growth factors in the fractone model. The only constraint placed on these values is that the threshold value must be less than the initial concentration.

Once the genomes are translated into their associated maps, they are evaluated by a function unique to the problem at hand and each member of the population is ranked based on their fitness. The most fit individuals are retained to repopulate the next generation of individuals by a combination of random mutation and cross-over of two parent genomes. The probabilities of crossover and mutation shall be cautiously selected by the user to ensure that the desirable characteristics are retained while allowing enough variation to avoid convergence at local optima. Once the offspring are generated, they are also evaluated for fitness and pooled together with the parent genomes. The combined population is ranked and the best genomes are selected to begin the next iteration. The process is completed when a prescribed number of iterations are achieved.

While a single objective optimization problem would be a straightforward example for

determining "fitness" in a genetic algorithm, it is often desired that a multiobjective optimization be performed. In this case there is a defined constraint:

$$g(x) \leq 0 \tag{2.9}$$

and a vector of objective functions to be minimized:

$$\{f_1(x), f_2(x), \cdots, f_n(x)\} \tag{2.10}$$

This problem is solved using a non-domination ranking system in which designs are preferred if they perform superior to other designs in one or more of the objective functions. Generally there is no single optimum design, and rather a Pareto front is formed. The points along the Pareto optimum are characterized such that one objective function cannot be improved without compensation in another target function. A niching scheme based on the proximity of points is also employed and promotes a greater spread of the Pareto front. The topological designs contained in or closest to the Pareto front are ranked higher and favored in the selection of parents for the next generation.

CHAPTER 3
RESULTS AND DISCUSSION

The previous section presented the methodologies for performing a topology optimization using a biologically inspired fractone model. In this section the results are presented for an optimization of the venation pattern for a flapping membrane wing of a micro air vehicle. Both the original map L-system topology generation and the fractone map L-system methods are employed and the resulting performances are compared. Some optimal wing designs and their performances are introduced here along with some analysis of the Pareto fronts generated during the optimizations.

3.1 Wing Design

The wing structure was composed of a thin latex membrane and a carbon fiber lattice structure. The membrane was characterized with an isotropic pre-stress condition and the carbon fiber beams were prescribed a rectangular cross-section. These details, along with the remaining material and geometric properties of the wing are presented in Table 3.1.

property	membrane	battens	leading edge
elastic modulus, E	2 MPa	300 GPa	300 GPa
Poisson's ratio, ν	0.5	0.34	0.34
density, ρ	1200 kg/m^3	1600 kg/m^3	1600 kg/m^3
thickness	0.1 mm	0.8 mm	2 mm
width	-	3 mm	5 mm
pre-stress, N_x, N_y	10 N/m	-	-

Table 3.1: Material and geometric properties of the membrane wing

The wing shape was defined with a root chord of 0.16 meters, a wing length of 0.4 meters, and a tip chord of 0.04 meters. A parabolic camber was prescribed with a maximum value of 2% the local chord length. There was no twist of the original wing, the dihedral angle was zero, and the angle of attack (α) was set to 4 °.

The kinematics of flight were parameterized with a flapping frequency (ω) of 40 rad/s

and a 30 ° amplitude of sinusoidal flapping (β). The flow velocity (U_∞) was 10 m/s and the density of air (ρ_∞) was 1.225 kg/m^3. The drag coefficients, C_{D0} and $C_{D\pi/2}$, were 0.05 and 2 respectively.

A number of parameters were also prescribed for the evaluation process which computed the fitness of each wing design. The structural analysis of the wings was performed with a finite element method using 20 modes. Airload analysis was performed with 20 span wise wing stations with 20 Gauss points and 6 inflow states. The flight dynamics were computed using a total of 100 timesteps per flapping cycle and 5 full cycles.

Three coefficients were defined for the multidisciplinary optimization of the wings. The lift generation, thrust generation, and power requirements were evaluated as follows:

$$C_L = -F_x/(0.5 \cdot \rho_\infty \cdot U_\infty^2 \cdot S)$$
$$C_P = P/(0.5 \cdot \rho_\infty \cdot U_\infty^3 \cdot S)$$
$$C_T = -F_y/(0.5 \cdot \rho_\infty \cdot U_\infty^2 \cdot S)$$

where F represents the respective forces, P is the accumulated power, and S is the area of the wing. For this optimization all coefficients were averaged over the flapping cycle and the lift coefficient was selected for the constraint function. The critical C_L value had a magnitude of 0.4892 (corresponding to a recorded average lift required for maximum thrust) and the constraint function was defined as:

$$g(x) = C_L - 0.4892 \tag{3.1}$$

The thrust and power coefficients were retained as the two objective functions (f_1(x), f_2(x)) to generate the Pareto fronts. A population size of 200 individuals and 200 generations were used in the genetic algorithm. The crossover probability of the genomes was 0.8 and the probability of mutation was 0.1.

The map L-system was constrained to a 20 letter alphabet and a maximum of 8 letters per production rule. A total of 4 iterations in the map generation were allowed. Growth

factor diffusion was assessed in the fractone map L-system with a fixed number and length of timesteps. A total of 5 timesteps were used in each iteration of the map generation and each step was uniform with a length of 0.1.

A large variety of skeletal designs were generated from the optimization schemes parameterized here. A glimpse at the diverse pool of the resulting topologies can be seen in figure 3.1. Here the most optimal designs for the power and thrust objective functions are displayed. Each set of structures were randomly selected from a fractone and non-fractone based optimization. The drastic differences in the power and thrust optimums are apparent as well as the similarities of results generated within each set. Both skeletal structures for optimal power coefficients contain very few members. The optimal design produced using the fractone system is especially sparse, while the design generated without fractones includes some reinforcement of the trailing edge. Similarly both designs for optimal thrust closely resemble each other with higher densities of the lattice structures and the majority of the members oriented span-wise.

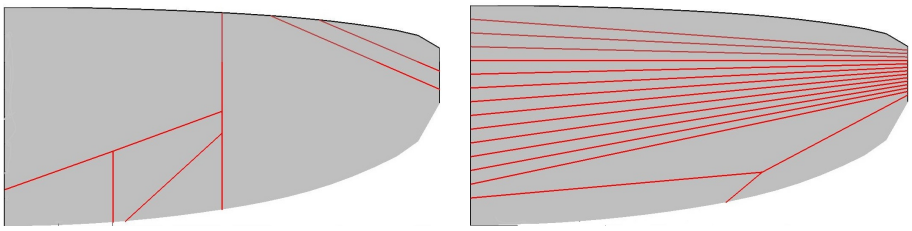

(a) Optimal power coefficient design without fractones: $C_{P,avg}$ = 0.3971, $C_{T,avg}$ = 0.1873, con_{avg} =0.0081

(b) Optimal thrust coefficient design without fractones: $C_{P,avg}$ =0.5270, $C_{T,avg}$ =0.2503, con_{avg} = $4.79e^{-4}$

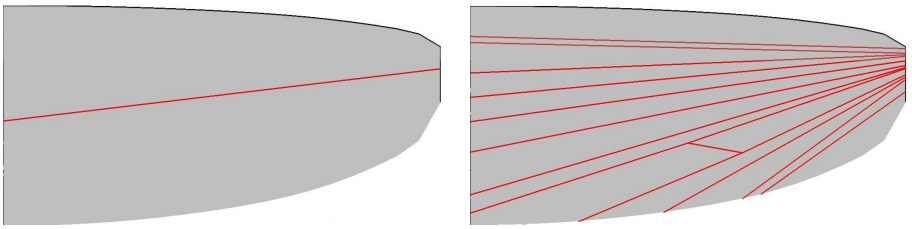

(c) Optimal power coefficient design using fractones: $C_{P,avg}$ =0.4085, $C_{T,avg}$ =0.1975, con_{avg} =0.0105

(d) Optimal thrust coefficient design using fractones: $C_{P,avg}$ =0.5142, $C_{T,avg}$ =0.2380, con_{avg} =0.0046

Figure 3.1: Optimal power and thrust coefficient designs

A selection of the resulting wings and their performances are presented in greater detail in figures 3.2 to 3.15. This collection includes a minimum power coefficient wing design resulting from the original map and fractone mapping systems in figures 3.2 and 3.9 respectively. An optimal thrust coefficient layout is also presented for the original and fractone mapping cases in figures 3.3 and 3.10 respectively. A total of five intermediate structures were also selected at random from each of the mapping scenarios and are displayed in figures 3.4 thru 3.8 and 3.11 through 3.15.

These results illustrate the structural dependence of the performances and correlate to the results found in [6]. As seen in the cases of the minimum power requirement designs, the lack of reinforcement at the trailing edge allowed for steeper gradients of displacement in the membranes. This allowed the wing a greater contour to the flow conditions and minimized the total power demand by reducing the aerodynamic resistance during both the upstroke and down-stroke of the flap. The compensation of this design however, was a reduction in peak thrust and lift performance. These designs (especially the fractone generated design with only one batten) had inferior lift performance to all other designs; while the lack of reinforcement allowed the wing to contour to more to flow, it reduced the occurrence of increased cambering and inflation.

In contrast to the power optimal designs, the stiffened thrust optimal designs exhibited reduced gradients with respect to the structures out-of-plane deformation. In both thrust optimal designs, the out-of-plane deformations were due to span-wise bending of the structures. During the down-stroke of these designs, when the lift was increased, it is seen that the angle of attack was also slightly reduced and this favored the generation of thrust.

Interesting results are also observed in the inspection of the random designs. In many of these scenarios, inflation occurred where venation was sparse and large deformation gradients were formed. Presumably these occurrences favored a lift optimal design. An interesting design is also seen in figure 3.13, in which chord wise reinforcements were incorporated. This design resulted in intermediate performance in all three design variables between the thrust and power optimal designs.

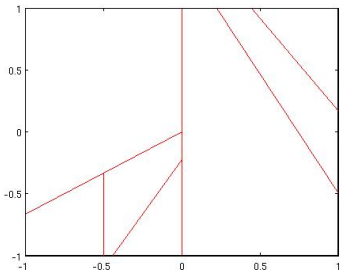

(a) Optimized map layout

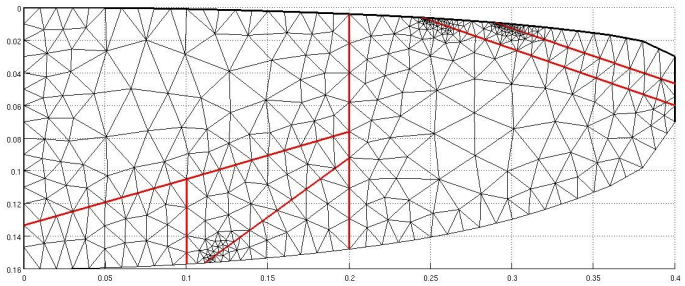

(b) Meshed wing structure

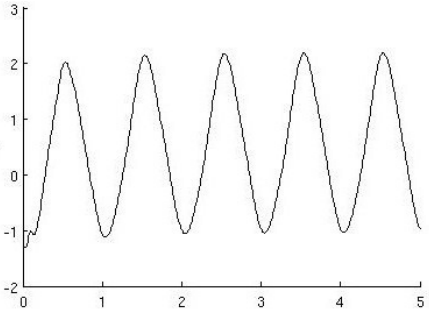

(c) Lift coeff vs. t/T , con_{avg} =0.0081

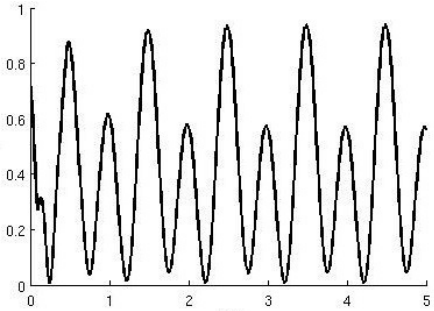

(d) Power coeff vs t/T, $C_{P,avg}$ =0.3971

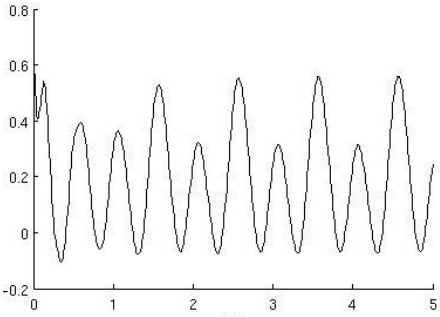

(e) Thrust coeff vs. t/T, $C_{T,avg}$ =0.1873

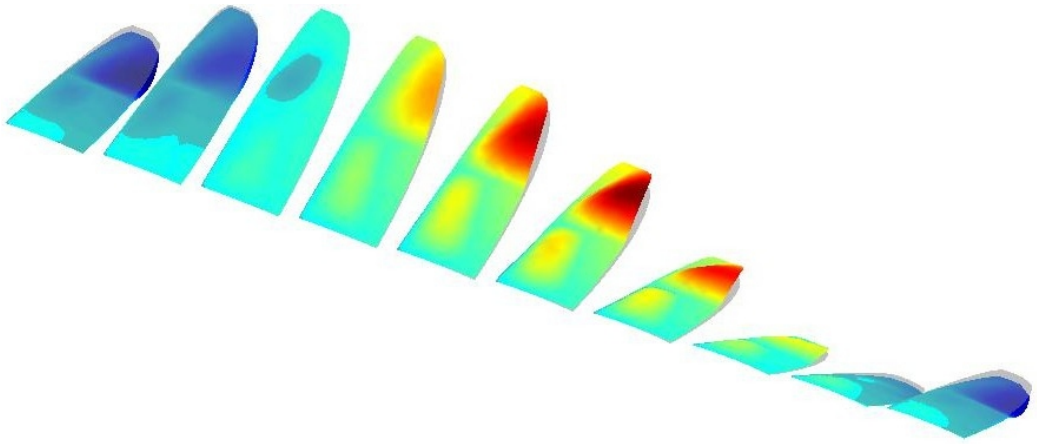

(f) Deformation of wing over a flapping cycle

Figure 3.2: Optimal power coefficient design: Original mapping system Run 1

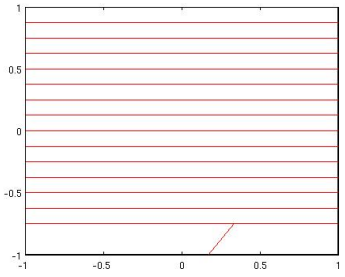

(a) Optimized map layout

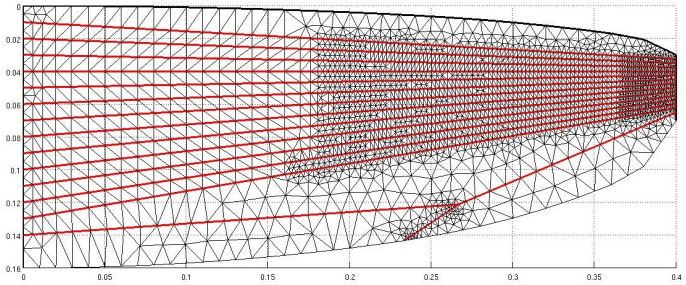

(b) Meshed wing structure

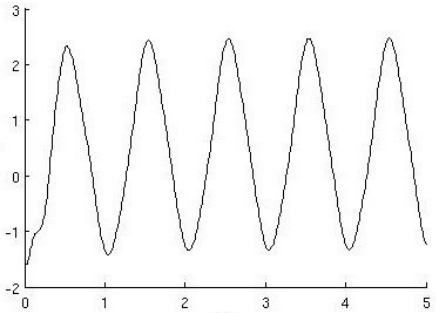

(c) Lift coeff vs. t/T , $con_{avg} = 4.79e^{-4}$

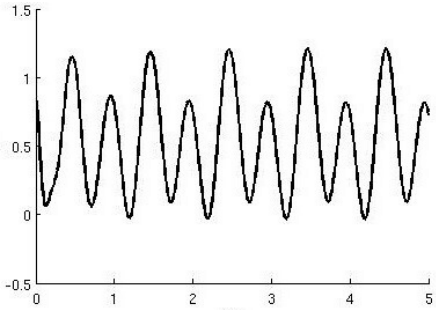

(d) Power coeff vs t/T, $C_{P,avg}$ =0.5370

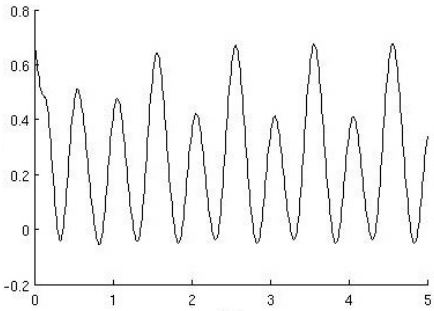

(e) Thrust coeff vs. t/T, $C_{T,avg}$ =0.2503

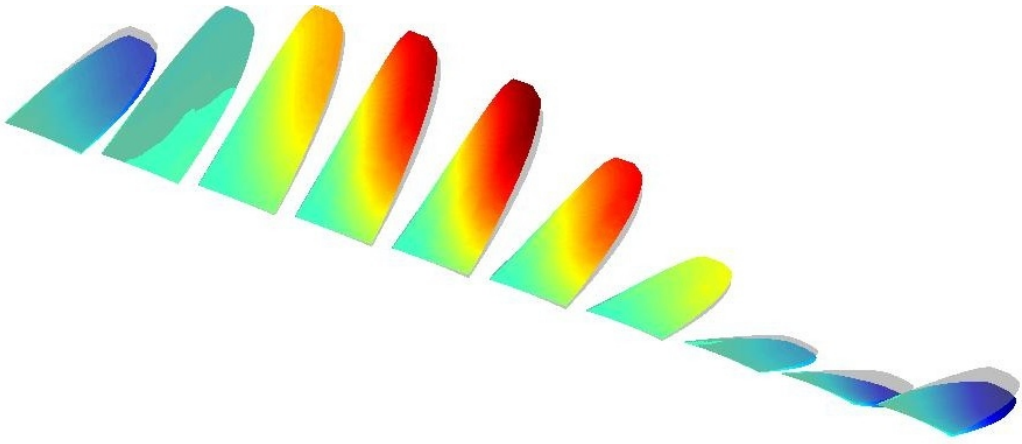

(f) Deformation of wing over a flapping cycle

Figure 3.3: Optimal thrust coefficient design: Original mapping system Run 1

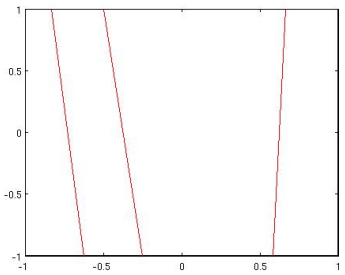

(a) Optimized map layout

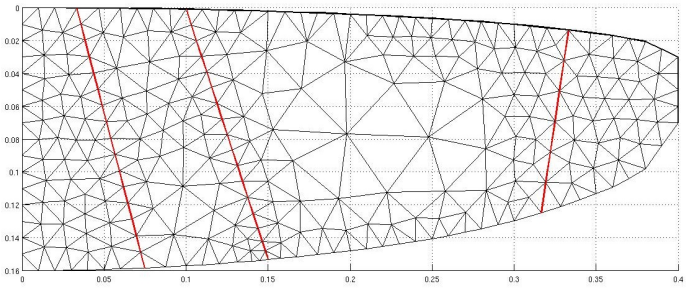

(b) Meshed wing structure

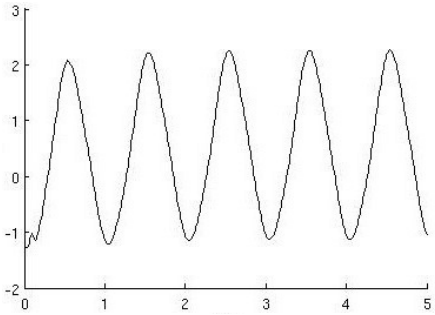

(c) Lift coeff vs. t/T , $con_{avg} = 0.0014$

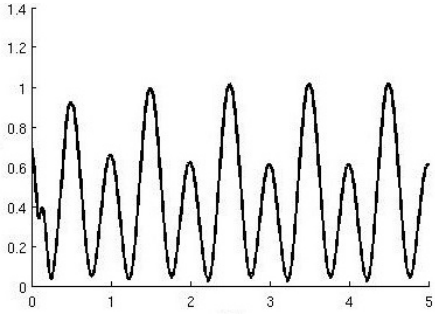

(d) Power coeff vs t/T, $C_{P,avg}$ =0.4325

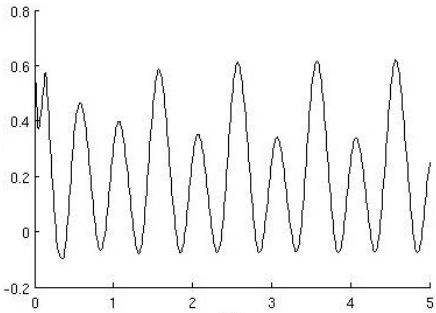

(e) Thrust coeff vs. t/T, $C_{T,avg}$ =0.2086

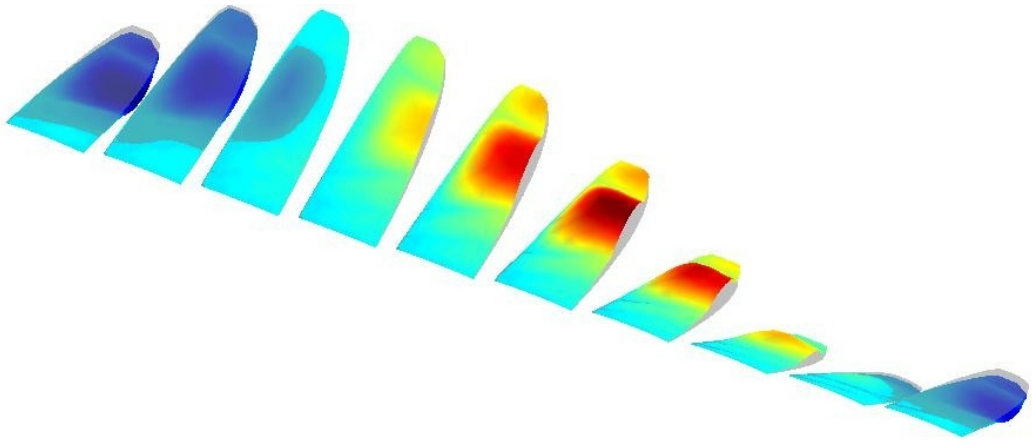

(f) Deformation of wing over a flapping cycle

Figure 3.4: Random design #1: Original mapping system Run 1

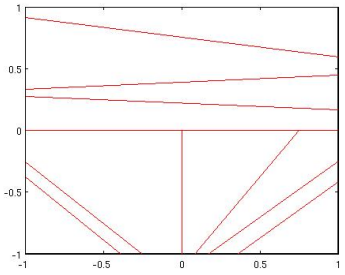

(a) Optimized map layout

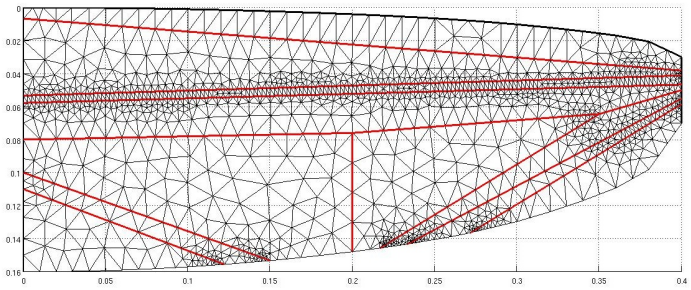

(b) Meshed wing structure

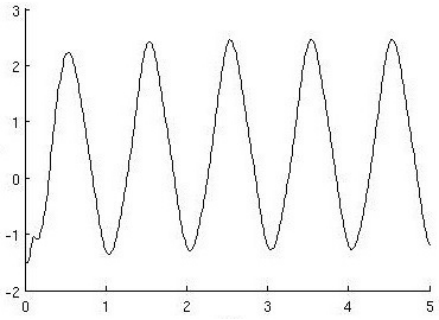

(c) Lift coeff vs. t/T , $con_{avg} = 0.0224$

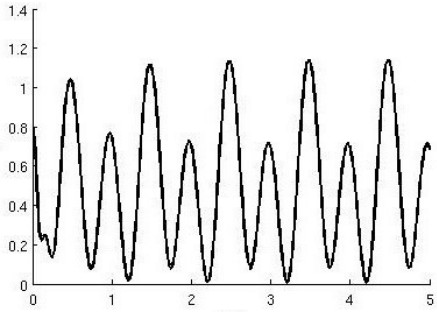

(d) Power coeff vs t/T, $C_{P,avg}$ =0.4936

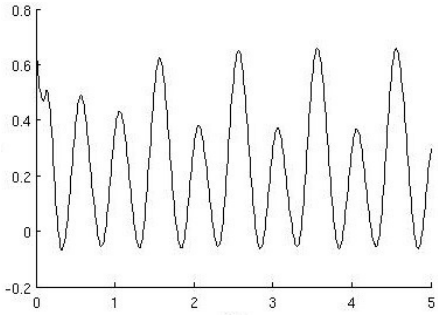

(e) Thrust coeff vs. t/T, $C_{T,avg}$ =0.2316

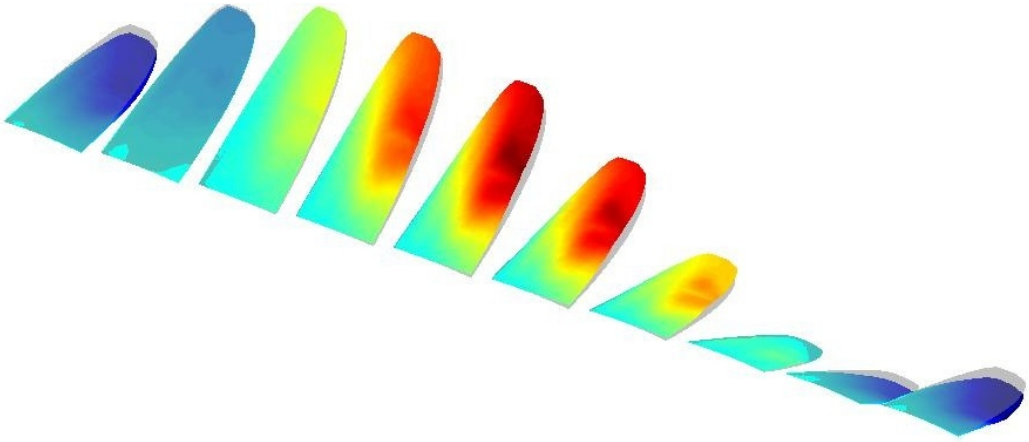

(f) Deformation of wing over a flapping cycle

Figure 3.5: Random design #2: Original mapping system Run 1

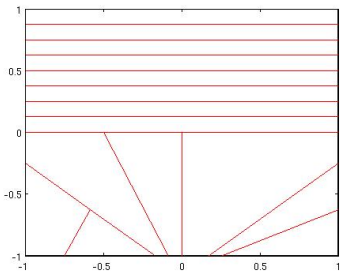

(a) Optimized map layout

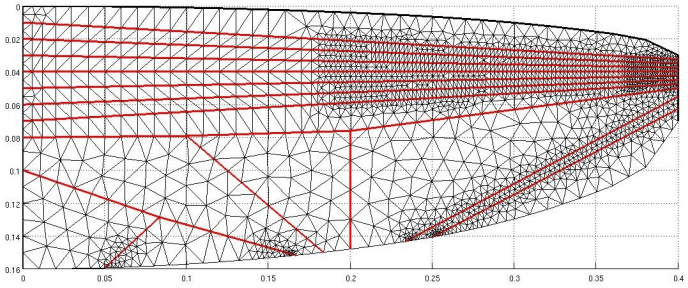

(b) Meshed wing structure

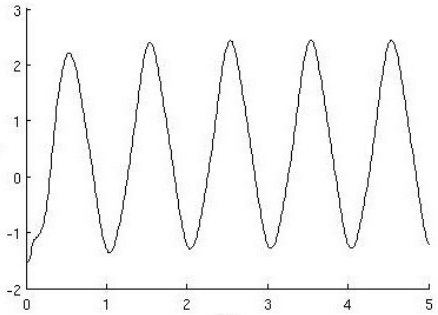

(c) Lift coeff vs. t/T , $con_{avg} = 0.0081$

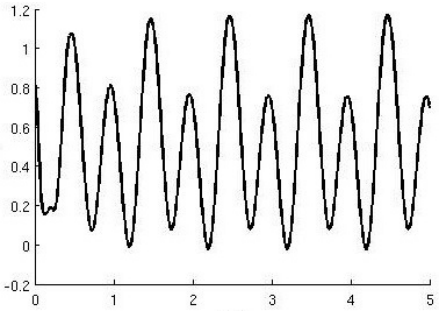

(d) Power coeff vs t/T, $C_{P,avg}$ =0.5039

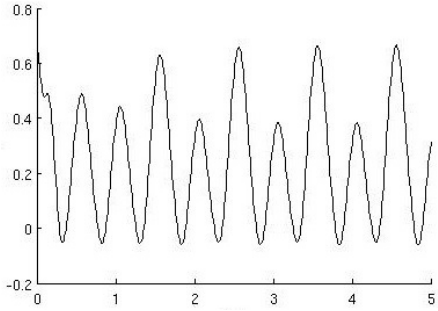

(e) Thrust coeff vs. t/T, $C_{T,avg}$ =0.2371

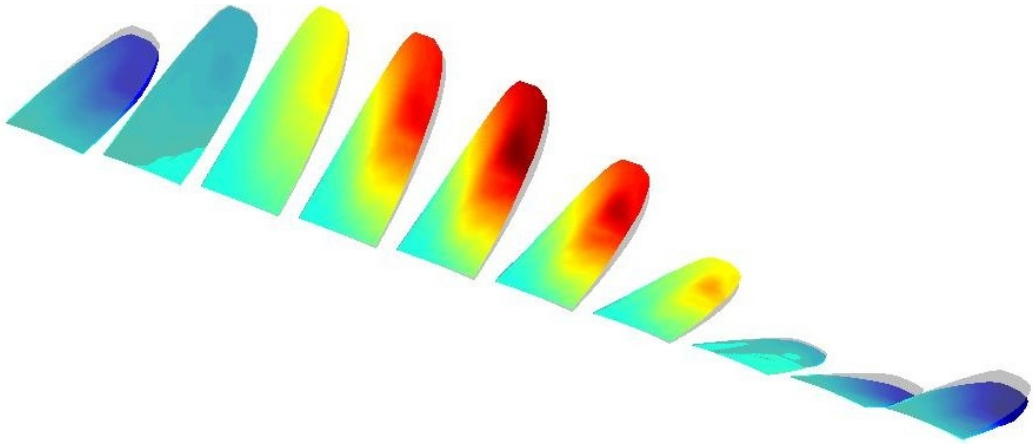

(f) Deformation of wing over a flapping cycle

Figure 3.6: Random design #3: Original mapping system Run 1

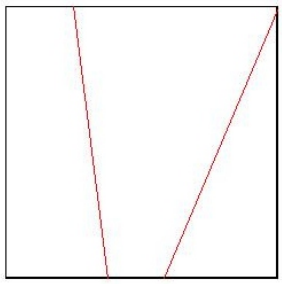

(a) Optimized map layout

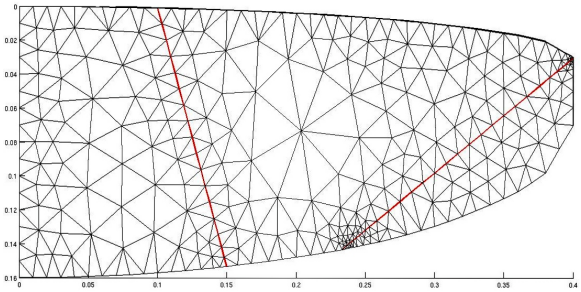

(b) Meshed wing structure

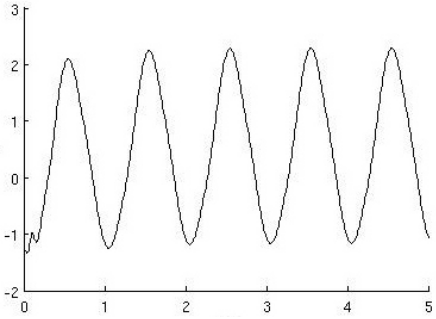

(c) Lift coeff vs. t/T , $con_{avg} = 0.0034$

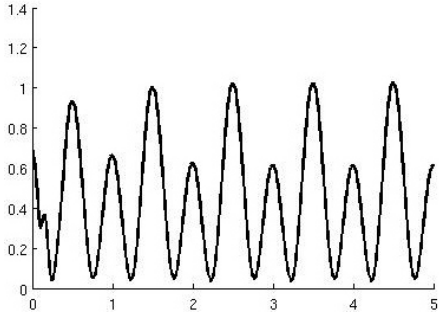

(d) Power coeff vs t/T, $C_{P,avg}$ =0.4390

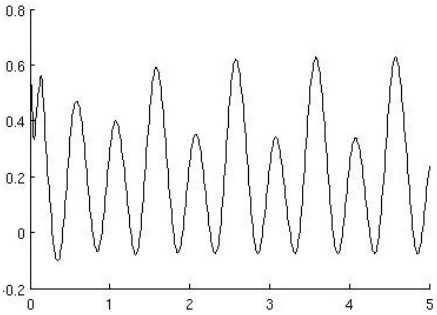

(e) Thrust coeff vs. t/T, $C_{T,avg}$ =0.2120

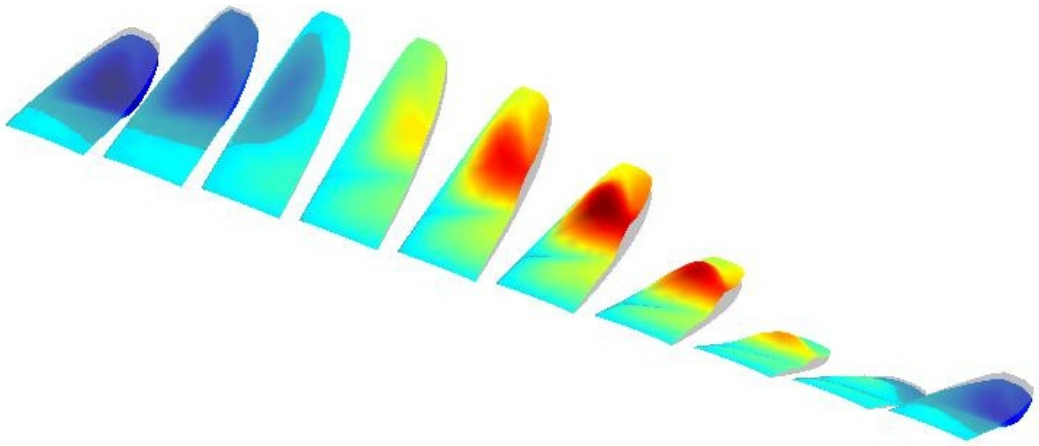

(f) Deformation of wing over a flapping cycle

Figure 3.7: Random design #4: Original mapping system Run 1

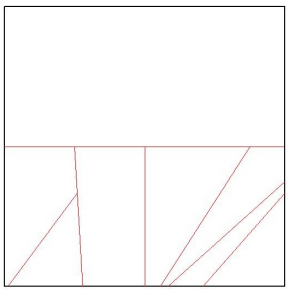

(a) Optimized map layout

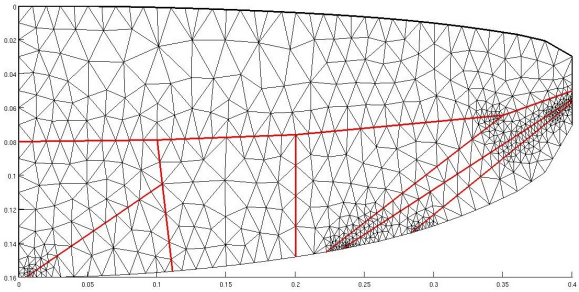

(b) Meshed wing structure

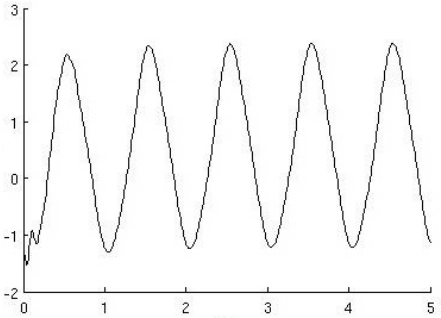

(c) Lift coeff vs. t/T , $con_{avg} = 0.0099$

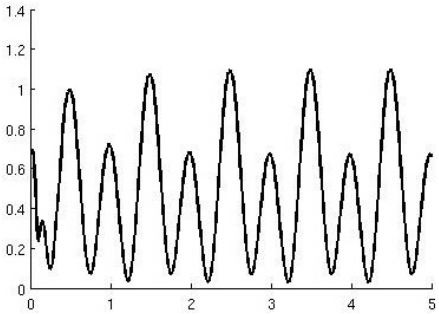

(d) Power coeff vs t/T, $C_{P,avg}$ =0.4750

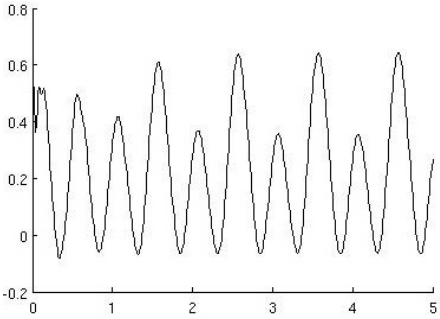

(e) Thrust coeff vs. t/T, $C_{T,avg}$ =0.2235

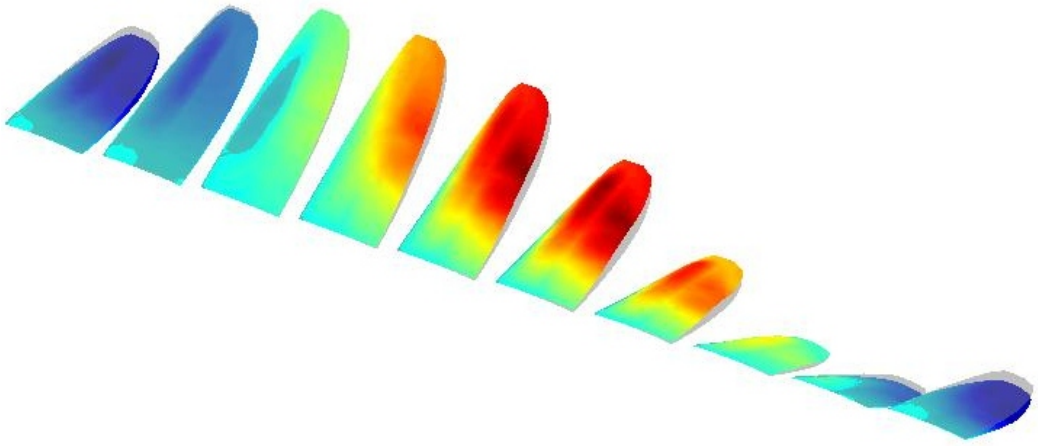

(f) Deformation of wing over a flapping cycle

Figure 3.8: Random design #5: Original mapping system Run 1

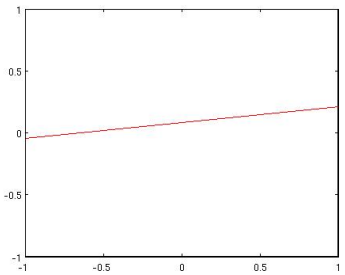

(a) Optimized map layout

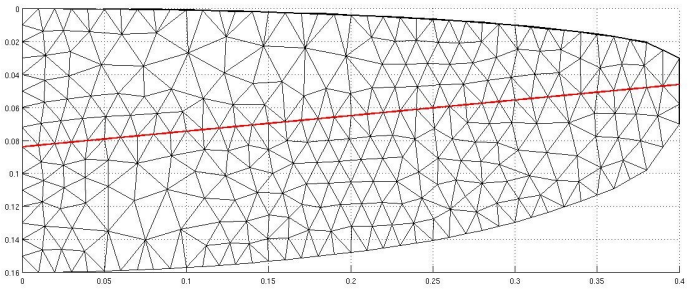

(b) Meshed wing structure

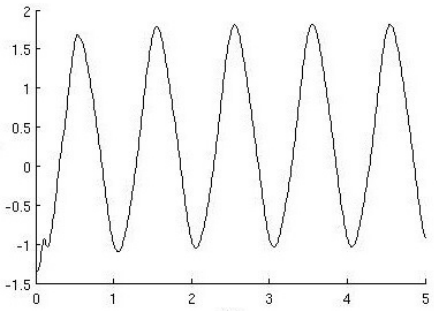

(c) Lift coeff vs. t/T , con_{avg} =0.0105

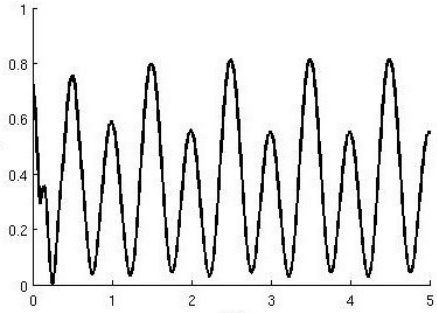

(d) Power coeff vs. t/T, $C_{P,avg}$ =0.4085

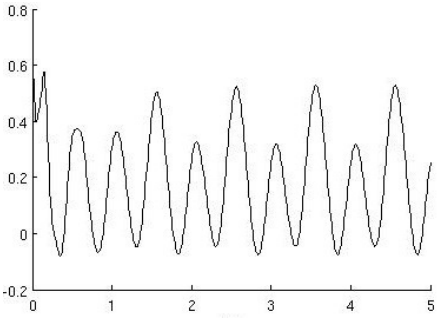

(e) Thrust coeff vs. t/T, $C_{T,avg}$ =0.1975

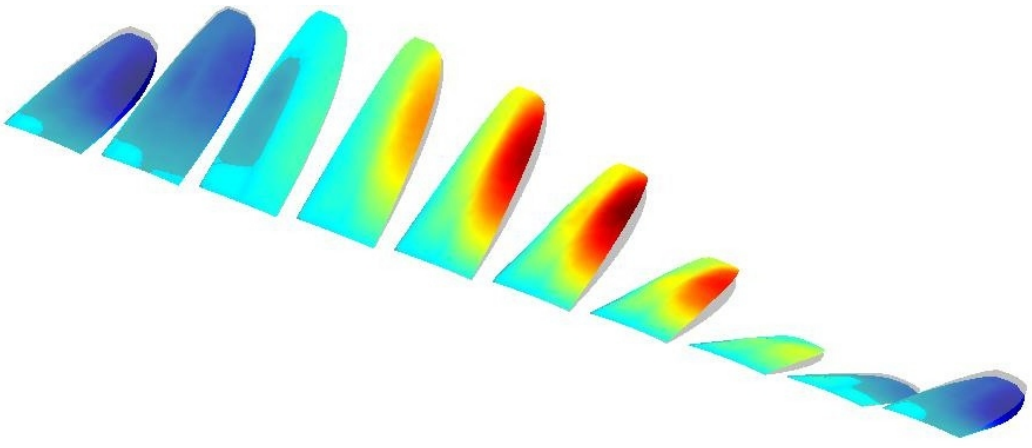

(f) Deformation of wing over a flapping cycle

Figure 3.9: Optimal power coefficient design: Fractone mapping system Run 2

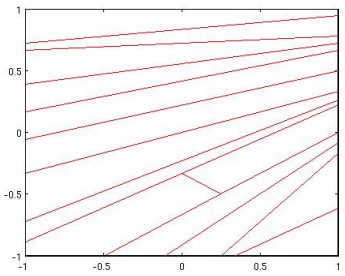

(a) Optimized map layout

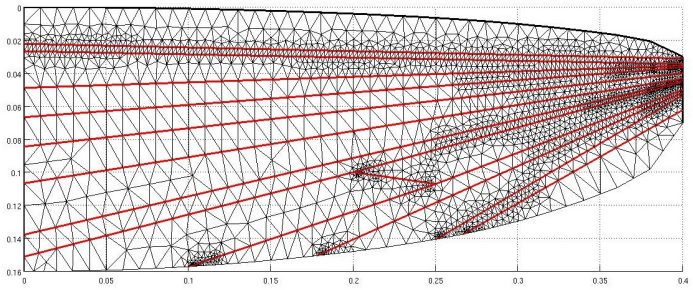

(b) Meshed wing structure

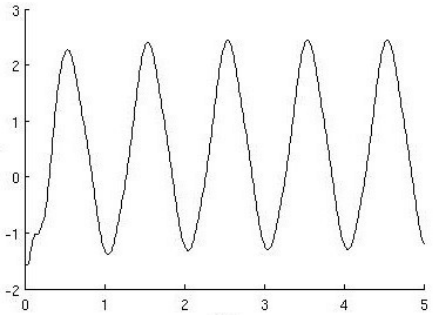

(c) Lift coeff vs. t/T , con_{avg} =0.0046

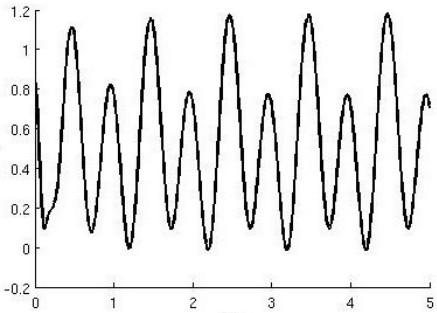

(d) Power coeff vs. t/T, $C_{P,avg}$ =0.5142

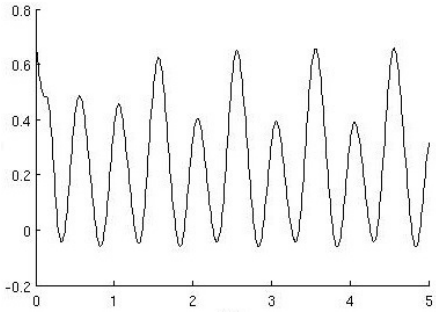

(e) Thrust coeff vs. t/T, $C_{T,avg}$ =0.2380

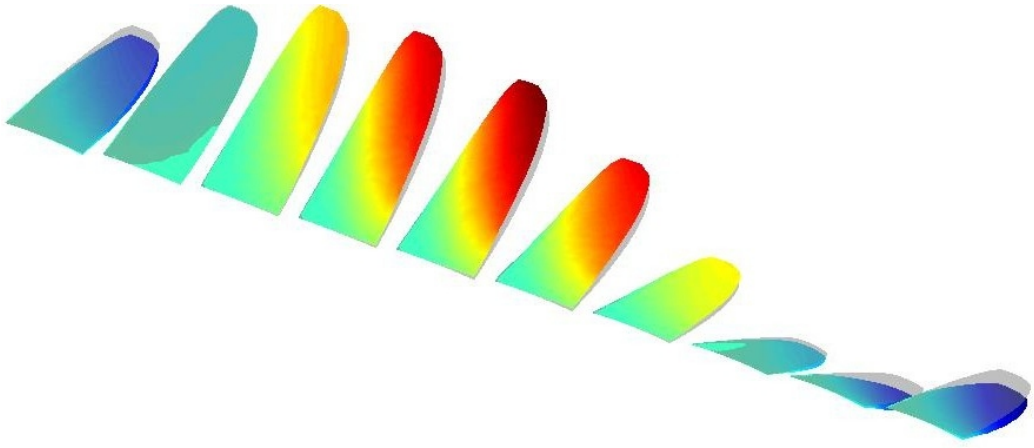

(f) Deformation of wing over a flapping cycle

Figure 3.10: Optimal thrust coefficient design: Fractone mapping system Run 2

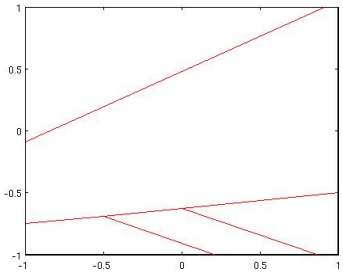

(a) Optimized map layout

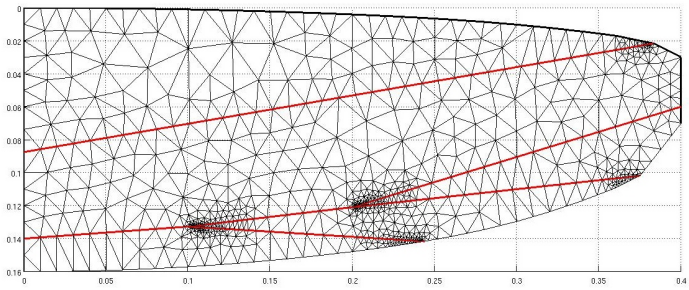

(b) Meshed wing structure

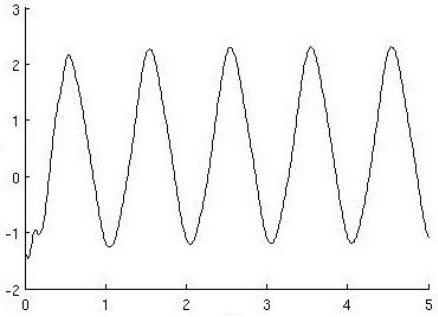

(c) Lift coeff vs. t/T , con_{avg} =0.0807

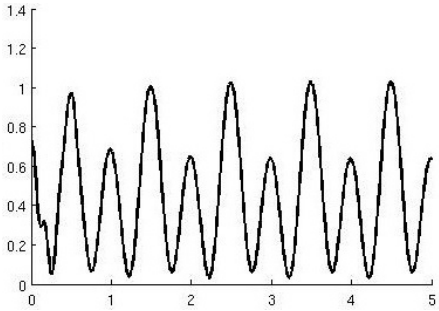

(d) Power coeff vs. t/T, $C_{P,avg}$ =0.4489

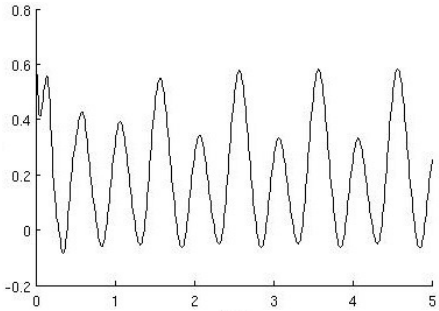

(e) Thrust coeff vs. t/T, $C_{T,avg}$ =0.2141

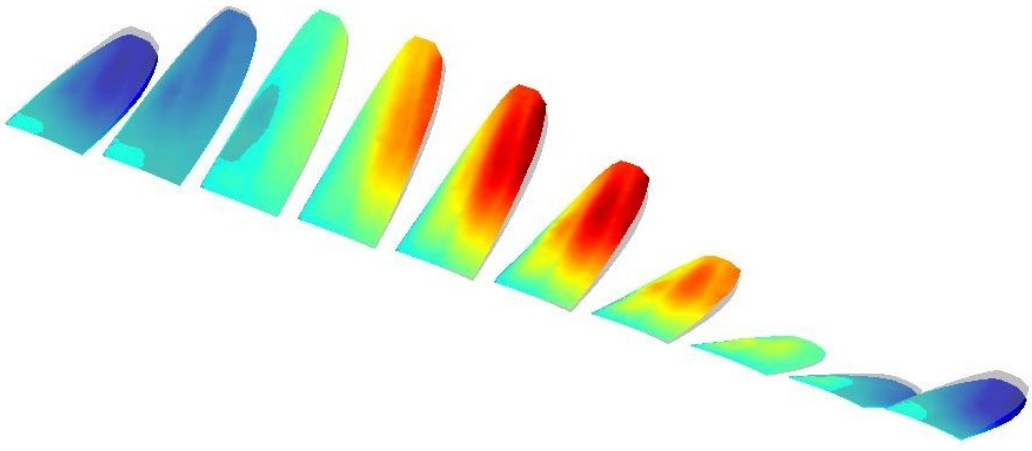

(f) Deformation of wing over a flapping cycle

Figure 3.11: Random Design #1: Fractone mapping system Run 2

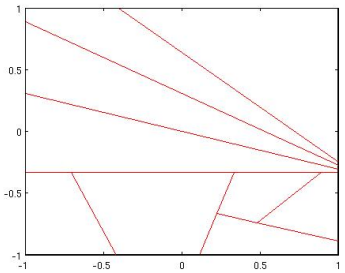

(a) Optimized map layout

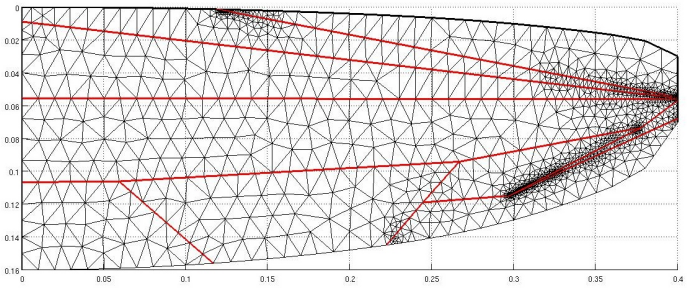

(b) Meshed wing structure

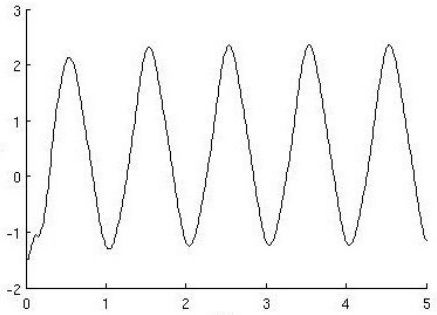

(c) Lift coeff vs. t/T , con_{avg} =0.0114

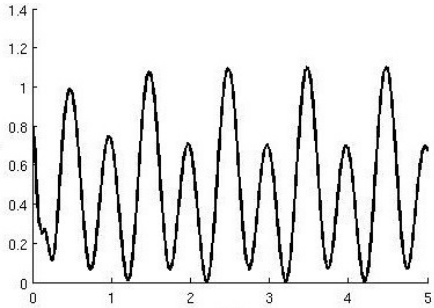

(d) Power coeff vs. t/T, $C_{P,avg}$ =0.4726

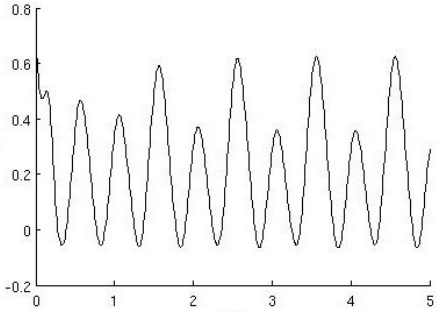

(e) Thrust coeff vs. t/T, $C_{T,avg}$ =0.2220

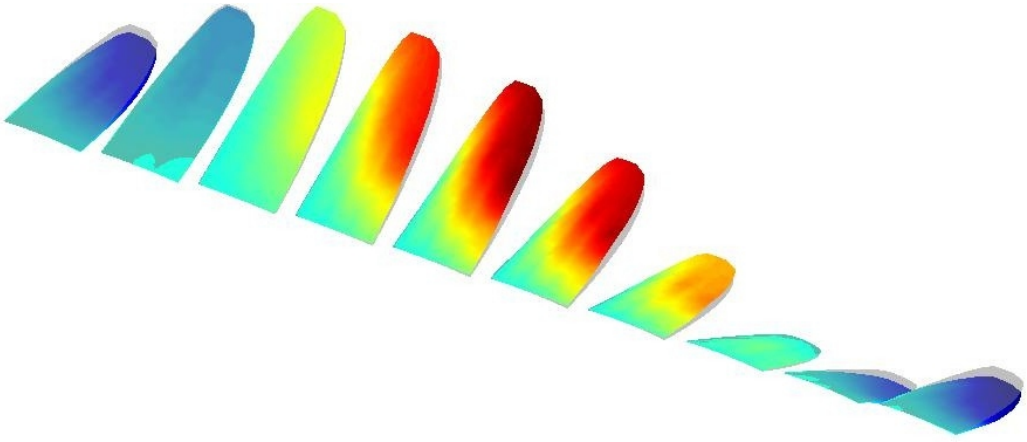

(f) Deformation of wing over a flapping cycle

Figure 3.12: Random Design #2: Fractone mapping system Run 2

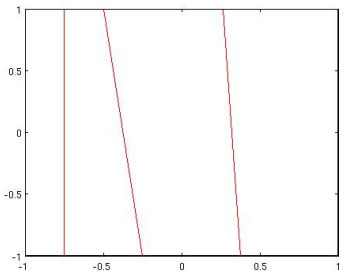

(a) Optimized map layout

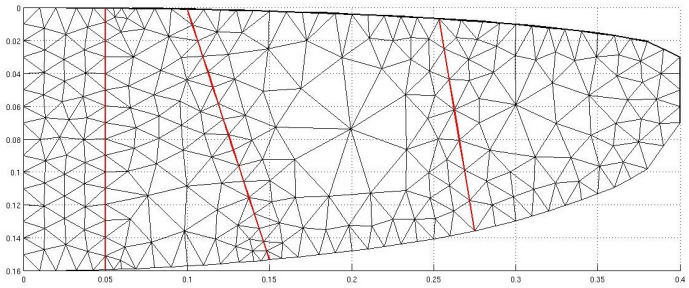

(b) Meshed wing structure

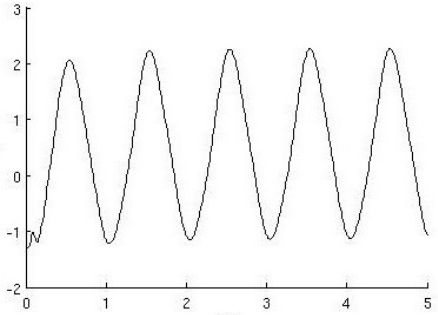

(c) Lift coeff vs. t/T , con_{avg} =0.0017

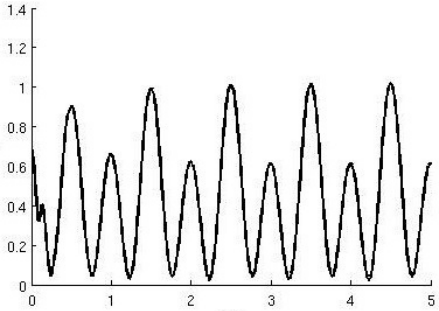

(d) Power coeff vs. t/T, $C_{P,avg}$ =0.4321

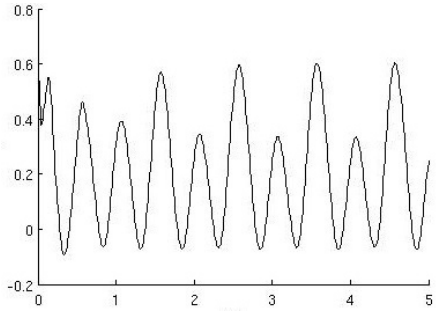

(e) Thrust coeff vs. t/T, $C_{T,avg}$ =0.2051

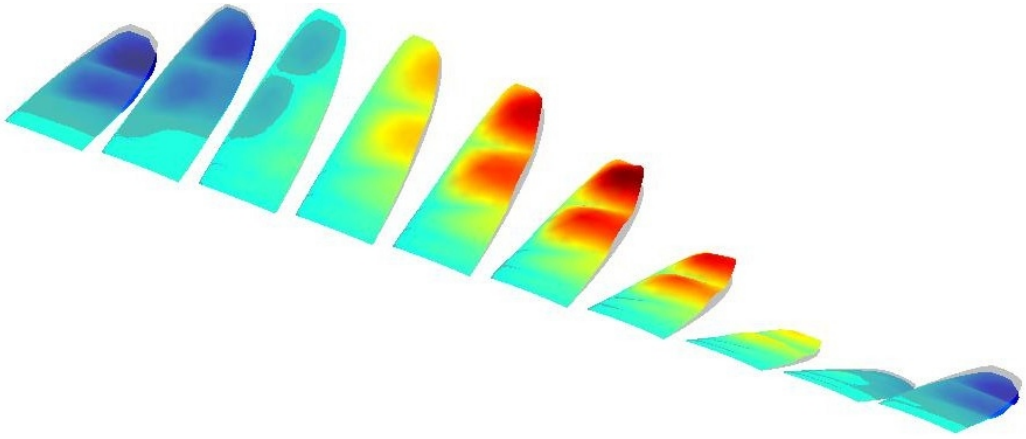

(f) Deformation of wing over a flapping cycle

Figure 3.13: Random Design #3: Fractone mapping system Run 2

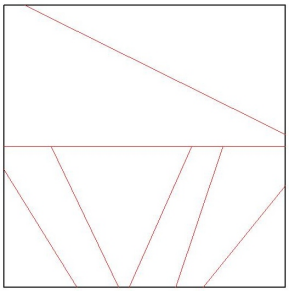

(a) Optimized map layout

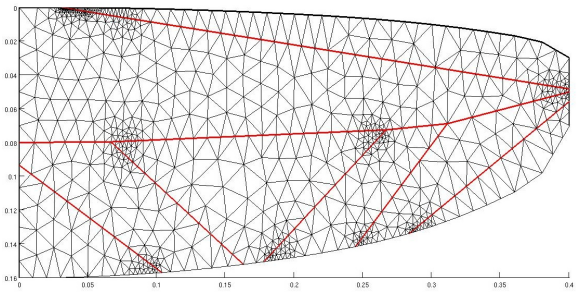

(b) Meshed wing structure

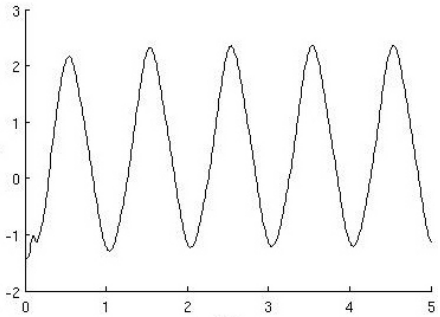

(c) Lift coeff vs. t/T , con_{avg} =0.0043

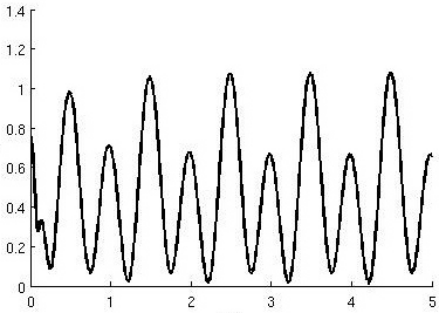

(d) Power coeff vs. t/T, $C_{P,avg}$ =0.4640

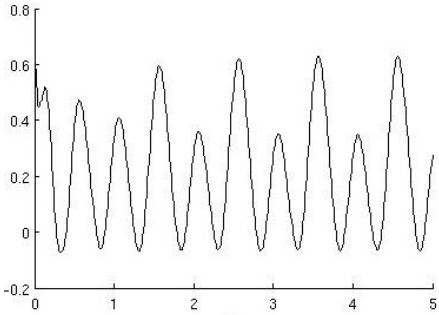

(e) Thrust coeff vs. t/T, $C_{T,avg}$ =0.2168

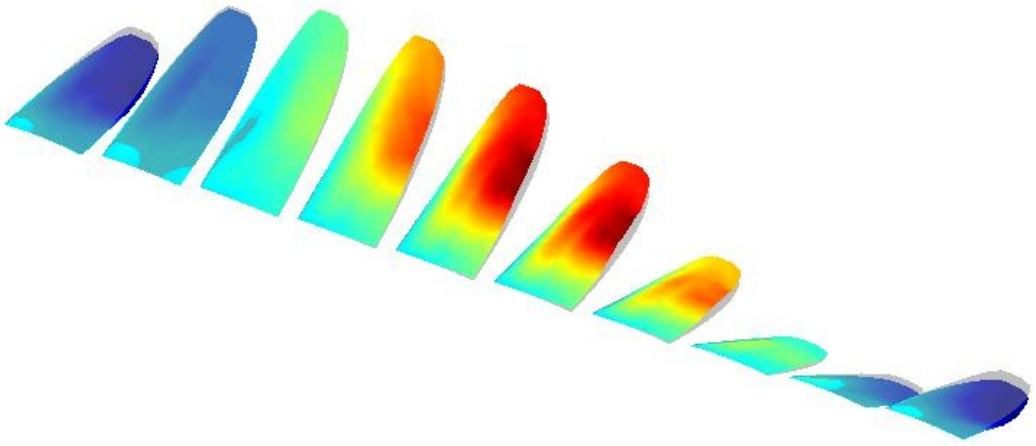

(f) Deformation of wing over a flapping cycle

Figure 3.14: Random Design #4: Fractone mapping system Run 2

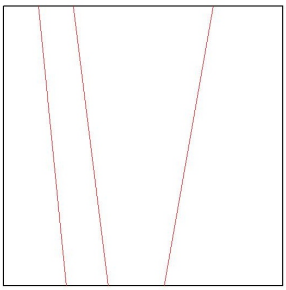

(a) Optimized map layout

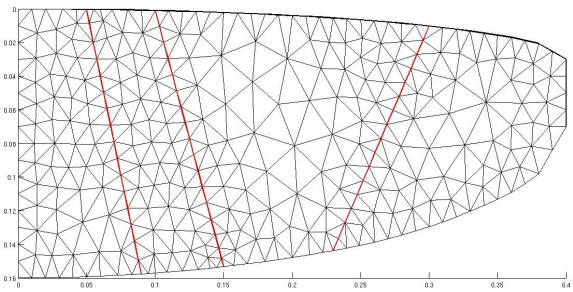

(b) Meshed wing structure

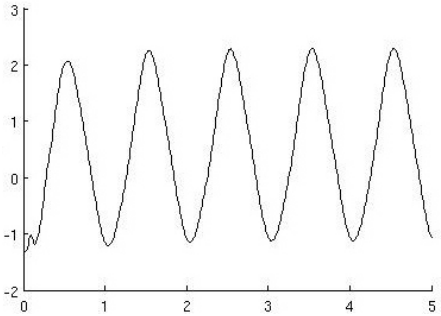

(c) Lift coeff vs. t/T , con_{avg} =0.0153

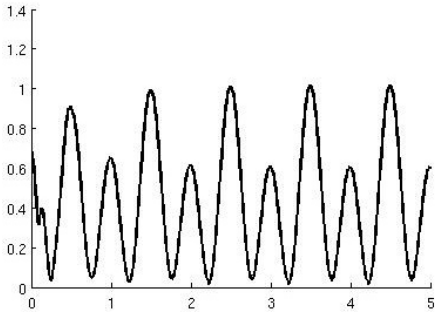

(d) Power coeff vs. t/T, $C_{P,avg}$ =0.4285

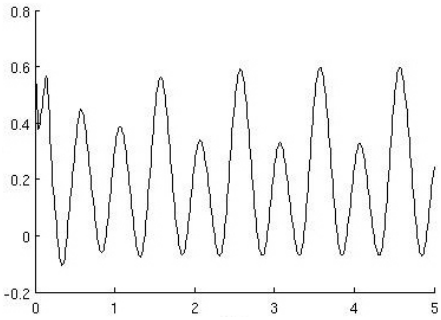

(e) Thrust coeff vs. t/T, $C_{T,avg}$ =0.2021

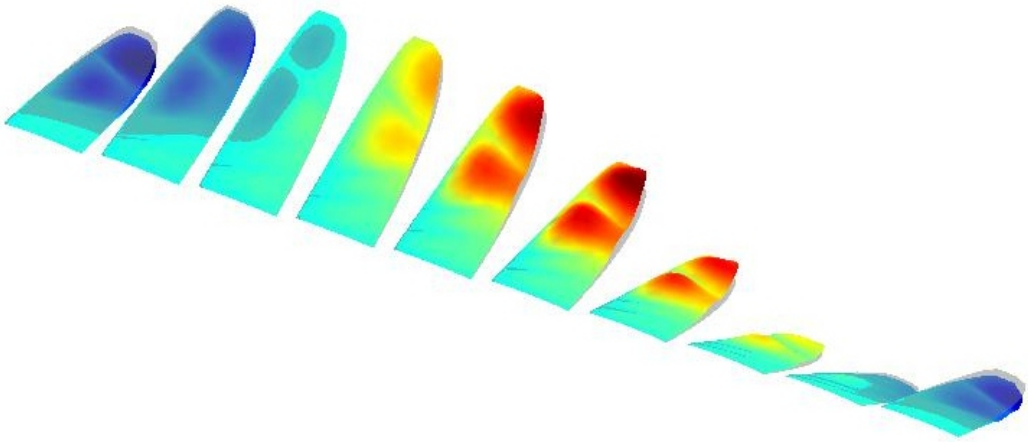

(f) Deformation of wing over a flapping cycle

Figure 3.15: Random Design #5: Fractone mapping system Run 2

3.2 Pareto Front Analysis

A total of ten trials were performed for each of the fractone and non-fractone optimizations. A typical Pareto front resulting in the final (200th) generation can be seen in figure 3.16. The Pareto front exhibited here illustrates a wide distribution of points as biased by the niching technique and superior performance of individuals compared to the other random designs.

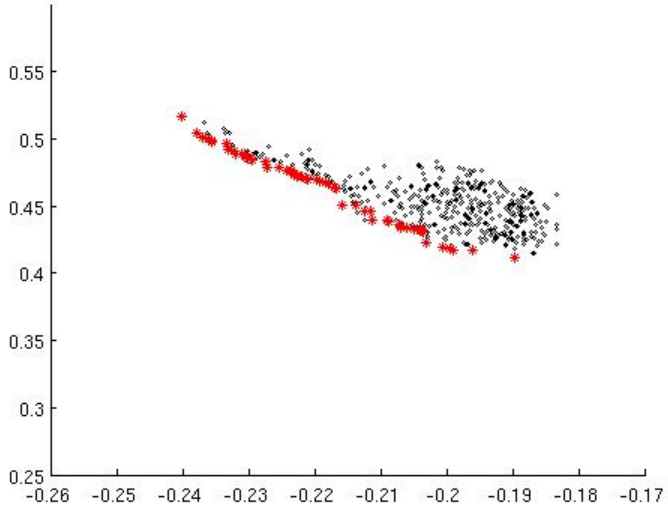

Figure 3.16: Sample Pareto Front (obtained from Run 2 without fractones):- Power coefficient vs. Thrust Coefficient, Pareto front (red) and other random designs (black)

3.2.1 Repeatability and Performance

The Pareto fronts obtained in the final generation of each of the ten trials were collected to observe the repeatability of the algorithm. Figure 3.17 displays the repeatability of results from both the fractone and original mapping schemes. The two different methods appear to have comparable performances in terms of repeatability as seen from the clustering of points and relatively narrow band-widths of the collected fronts.

The collection of Pareto fronts from the two methods were further combined in figure 3.18 to compare the performance of the two methods. The dispersion of points belonging to

the two cases is fairly even and consistent. No single method appears to perform drastically superior to the other since the two sets are clustered together rather than detached. Close inspection of the leading edge of the front (the lower-left edge of the collected points) however, appears to indicate a slight domination of the fractone model. A majority of the most optimal designs in this application belong to the fractone derived topologies.

3.2.2 Convergence

Determination of the rate of convergence for the Pareto fronts was first approximated with a plotting of Pareto fronts from each generation. This was completed for each of the twenty runs, however visual assessment of the point of convergence was difficult to determine. An example of one such plot can be seen in figure 3.19 in which the 200 generations were plotted using 5 colors to distinguish every set of 40 generations.

To better determine the convergence, the Pareto fronts were numerically approximated by computing an averaged norm. The minimum distances from each point in a Pareto front to the set of points in the 200th generation Pareto front were estimated and averaged for each approaching generation. Since the span of Pareto fronts varied over each generation, the points which exceeded the span of the final (200th) Pareto front were eliminated for this approximation for the convergence rate. The resulting convergence rates were compiled and can be seen in figure 3.20. Here the convergence rates appear to be comparable, however the rate of convergence with the fractone mapping scheme appears to be more variable between runs while the non-fractone mapping system converges with slightly better repeatability.

The convergence curves for each of the 10 runs were also averaged among both the fractone and original cases. The two curves are compared in figure 3.21. This graph illustrates that the averaged convergence rates for the fractone and non-fractone models are indeed comparable. Both models are rapidly improved over the first few generations as seen by the rapid decrease in the averaged distance between Pareto fronts. Both models are also nearly converged to the optimal designs by the 100th generation. The results presented in this figure seem to contradict the initial prediction that the fractone model may improve

the convergence rates of the optimization. It must be noted though, that the convergence rates were computed with respect to the Pareto fronts generated in each individual test run. These Pareto fronts have marginal differences and as seen in the previous subsection and the actual Pareto front of the fractone cases may be slightly more optimal.

Limited improvement in the convergence of the fractone model may be due to the parameters assigned to the mapping algorithm. As previously mentioned, the map L-system enforces a number of preceding requirements for the matching of markers. Since the fractone model must also satisfy all other preexisting rules for matching markers, including the requirement of similar character labels, the influence of the fractone model was greatly limited in this study.

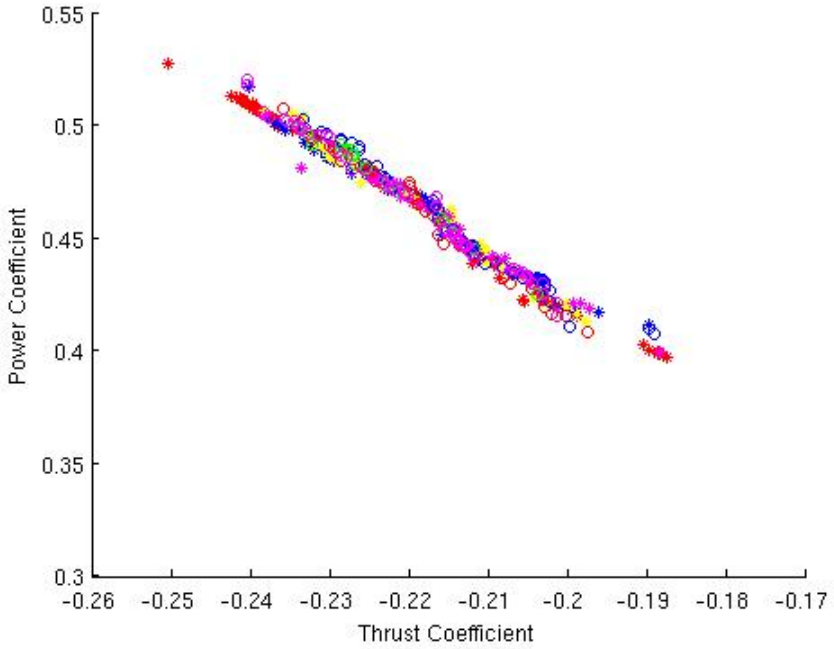

(a) Original mapping (no fractones)

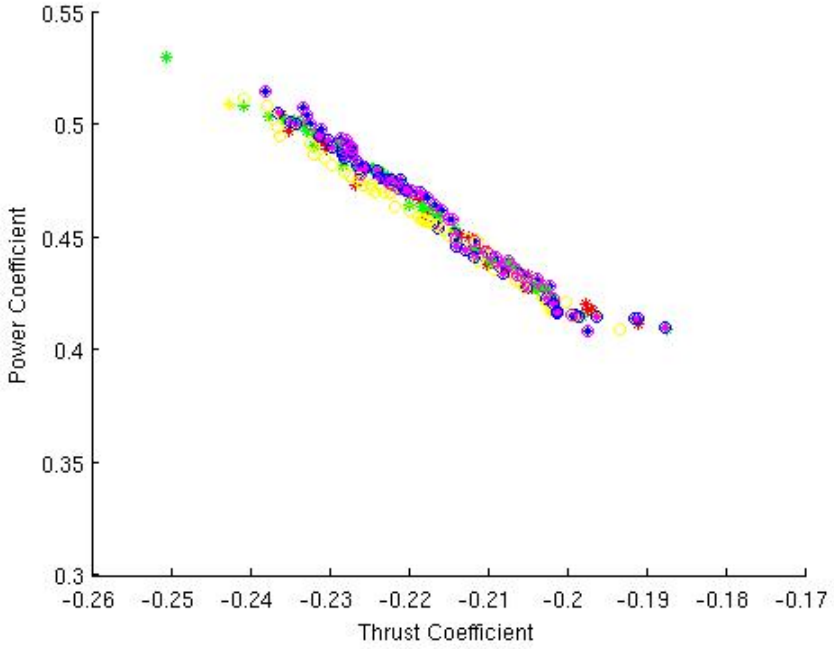

(b) Fractone mapping

Figure 3.17: Final Pareto fronts collected from runs 1 through10 (each test batch displayed in different colors and markers)

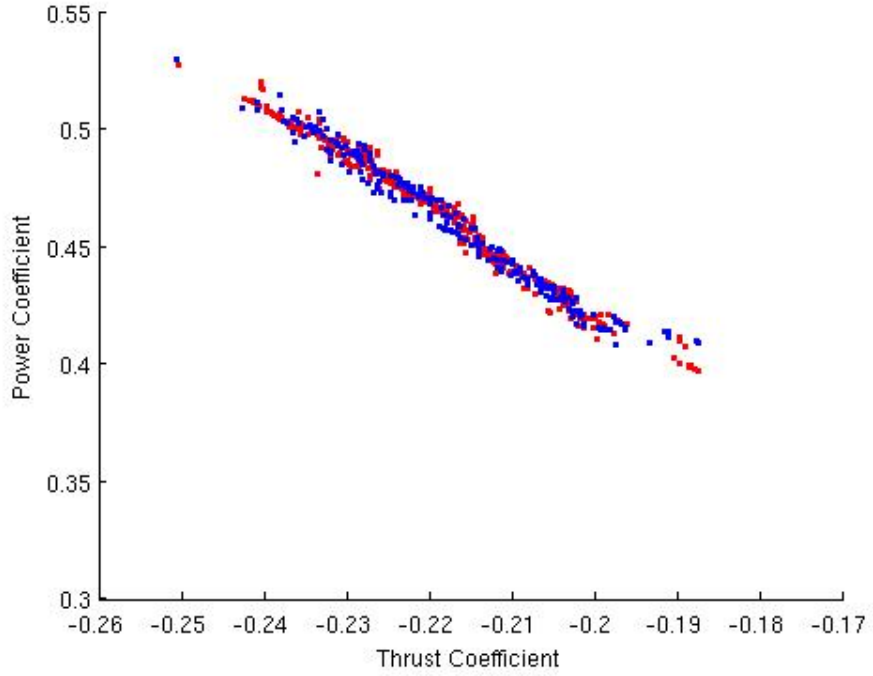

Figure 3.18: Collection of final Pareto fronts from 10 runs: fractone mapping in blue, original mapping in red

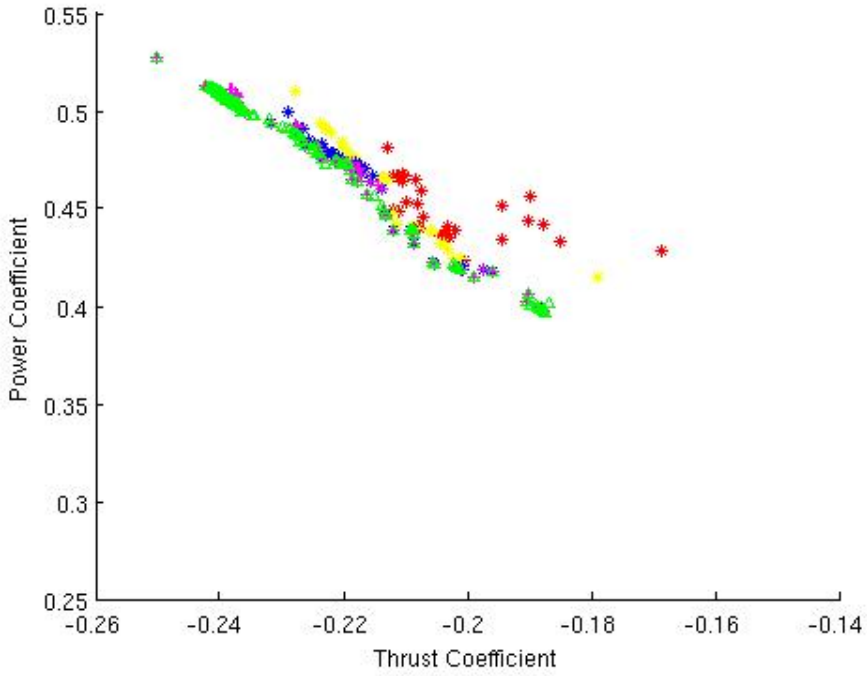

Figure 3.19: Visual assessment of convergence of Pareto fronts using 5 colors (Run 1 without fractones): Generations 1-40(red), 41-80(yellow), 81-120(blue), 121-160(pink), and 161-200 green)

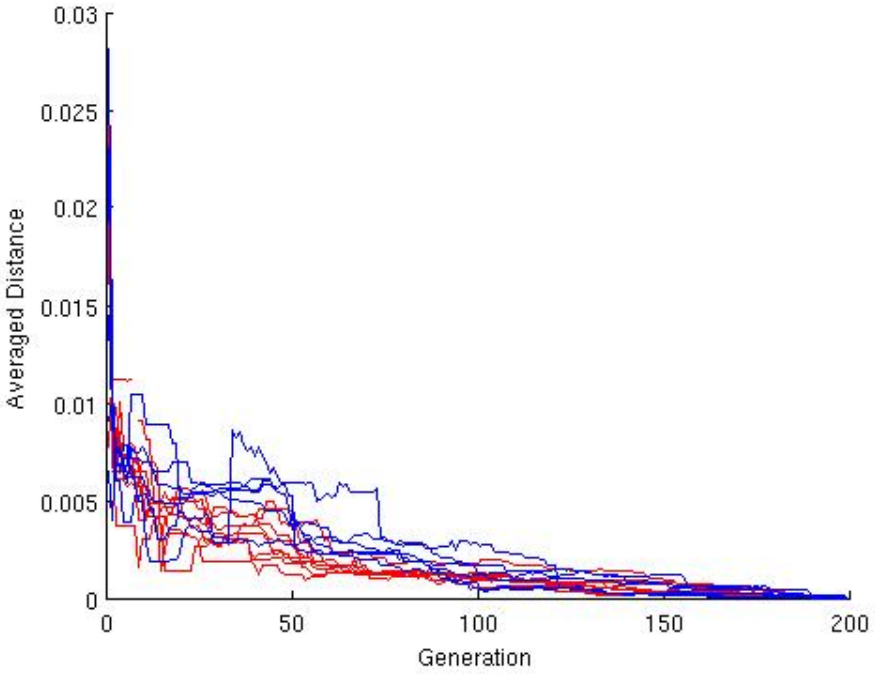

Figure 3.20: Convergence rates for 10 runs : fractone mapping in blue, original mapping in red

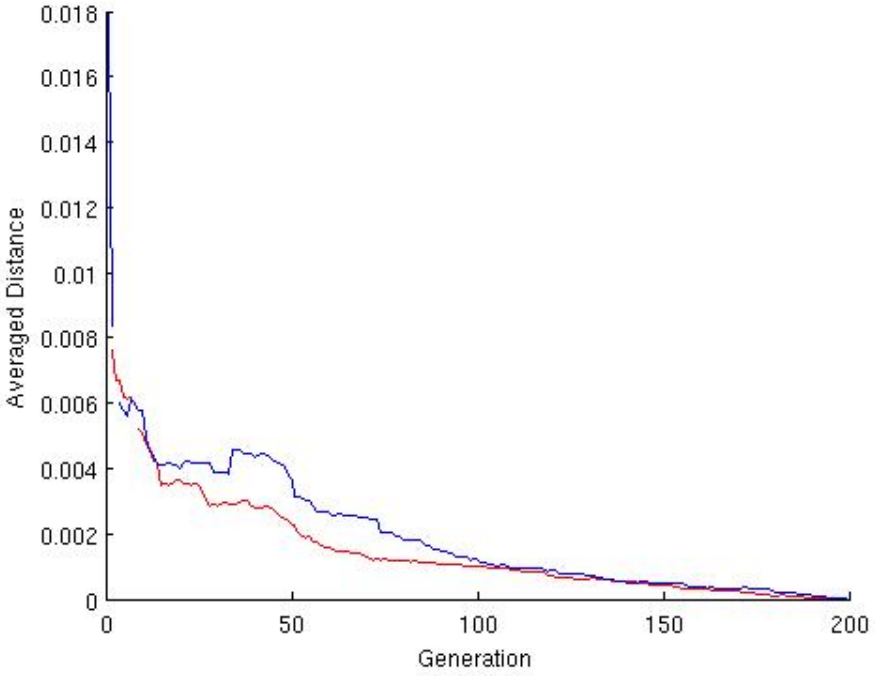

Figure 3.21: Averaged convergence rates for 10 runs: fractone mapping in blue, original mapping in red

CHAPTER 4
CONCLUSION

This work introduced a new method for topology optimization. The new approach adapted a topological mapping algorithm originally inspired by the cellular division process, and imposed the additional constraint of fractones. The modeling of growth factor diffusion and capture within the map L-system created an additional control parameter for optimization by the genetic algorithm.

The resulting multidisciplinary optimization method was tested with a flapping membrane wing problem in which the layout of reinforcement members was improved. The topologies generated in this application were optimized for average lift generation, thrust generation, and power requirements of the wing structures under a prescribed flight condition. The resulting Pareto fronts and wing performances were analyzed and interesting findings were made.

A wide variety of wing topologies were generated from the optimization process and the range of the venation patterns were found to produce uniquely different performances during flight. Similarities among the power and thrust optimal designs were also found. The power optimal designs were generally less structured so that the wings were allowed to contour to the flow and minimize the aerodynamic resistance. The thrust optimal designs on the other hand had much higher densities of span-wise reinforcements which caused gradual deformations along the wing structure during flight.

While the venation patterns generated from the optimizations produced great diversity and successful results, the performances of the two optimization methods themselves showed less variation. The Pareto fronts generated by the fractone inspired method and the original map L-system method were analyzed for fitness, repeatability, and convergence. Comparisons of the two optimization approaches were made and little difference was found between the two in all three categories of performance. The lack of effectiveness from the fractone model is predicted to arise from the layers of requirements placed on the matching

of markers in the mapping systems.

4.1 Future Work

As earlier mentioned, it would be desirable to repeat the methods presented here with a modification to the mapping system. Since a number of other requirements are imposed by the map L-system in the matching of markers, it may desirable to place fractones only where the eligible (matching label and orientation) markers are located. Enforcement of the fractone and diffusion model after the eligible matching marker pairs of the map L-system are found may increase the influence of the fractone method. Evaluation of the resulting model may then be used to once again assess the effect of fractones on convergence rates and topological designs.

Other future testing may include variation of the cross-over and mutation probabilities in the genetic algorithm to determine the influence of each parameter independently. Further modifications of the fractone model may also be made. While this study considered a constant distribution of growth factors along the perimeters of the edges, the method may be further improved by encoding a non-uniform distribution in the genome of the mapping system as well. Variations of the fractones themselves are also possible. In this study the fractones remained active once they were formed and continued to consume the diffusing growth factors, however they may also be inactivated once the mapping iteration is completed and new fractones are placed.

BIBLIOGRAPHY

[1] Martin P. Bendsøe and Ole Sigmund. Material interpolation schemes in topology optimization. *Archive of Applied Mechanics*, 69:635—654, 1999.

[2] G. I. N. Rozvany. Aims, scope, methods, history and unified terminology of computer-aided topology optimization in structural mechanics. *Structural and Multidisciplinary Optimization*, 21, 2001.

[3] C. D. Chapman; K. Saitou; M. J. Jakiela. Genetic algorithms as an approach to configuration and topology design. *Journal of mechanical design*, 116(4):1005–1012, 1994.

[4] O. Sigmund and J. Petersson. Numerical instabilities in topology optimization: A survey on procedures dealing with checkerboards, mesh-dependencies and local minima. *Structural and Multidisciplinary Optimization*, 16:68–75, 1998. 10.1007/BF01214002.

[5] M. H. Kobayashi; H-T. C. Pedro; R. M. Kolonay and G. W. Reich. On a cellular division method for aircraft structural design. *The Aeronautical Journal of the Royal Aeronautical Society*, 113(1150):821–831, 2009.

[6] Philip Beran Bret Stanford and Marcelo Kobayashi. Aeroelastic optimization of flapping wing venation: A cellular division approach. In *AIAA 2011-2094*, 2011.

[7] Aurelien Kerever, Jason Schnack, Dirk Vellinga, Naoki Ichikawa, Chris Moon, Eri Arikawa-Hirasawa, Jimmy T. Efird, and Frederic Mercier. Novel extracellular matrix structures in the neural stem cell niche capture the neurogenic factor fibroblast growth factor 2 from the extracellular milieu. *STEM CELLS*, 25(9):2146–2157, 2007.

[8] Frederic Mercier, John T. Kitasako, and Glenn I. Hatton. Fractones and other basal laminae in the hypothalamus. *The Journal of Comparative Neurology*, 455(3):324–340, 2003.

[9] John Rader Vanessa Douet Eri Arikawa-Hirasawa Youngsu Chow Kwon Monique Chyba, Frederic Mercier and Rich Kodama. Dynamic mathematical modeling of cell-fractone interactions. *Journal of Math-for-Industry*, 3:79–88, 2011.

[10] Przemyslav Prusinkiewicz and Aristid Lindenmayer. *The Algorithmic Beauty of Plants*. Springer Verlag, New York, 2004.

[11] A. Nakamura, A. Lindenmayer, and K. Aizawa. *The Book of L*, chapter Some Systems for Map Generation, pages 323—332. Springer, Berln, 1986.

[12] W.M. Becker. *The World of the Cell*. Pearson/Benjamin Cummings, 2009.

[13] Graham F. Carey Eric B. Becker and J. Tinsley Oden. *Finite Elements An Introduction : Volume I*. Prentice Hall, New Jersey, 1981.